Electrical Imaging for Hydrogeology

Kamini Singha, Timothy C. Johnson, Frederick D. Day-Lewis, Lee D. Slater

THE
GROUNDWATER
PROJECT

Electrical Imaging for Hydrogeology

The Groundwater Project

Kamini Singha

Professor
Hydrologic Science and Engineering Program
Department of Geology and Geological Engineering
Colorado School of Mines
Golden, Colorado, USA

Timothy C. Johnson

Research Geophysicist
Energy and Environment Directorate
Pacific Northwest National Laboratory
Richland, Washington, USA

Frederick D. Day-Lewis

Chief Geophysicist
Energy and Environment Directorate
Pacific Northwest National Laboratory
Richland, Washington, USA

Lee D. Slater

Henry Rutgers Professor of Geophysics
Department of Earth and Environmental Sciences
Rutgers University
Newark, New Jersey, USA

Electrical Imaging for Hydrogeology

The Groundwater Project
Guelph, Ontario, Canada
Version 4, March 2023

ii

Groundwater Project (GW-Project) works are copyrighted and can be downloaded for free from gw-project.org↗. Anyone may use and share gw-project.org↗ links to download GW-Project's works. It is neither permissible to make GW-Project documents available on other websites nor to send copies of the documents directly to others. Kindly honor this source of free knowledge that benefits you and all those who want to learn about groundwater.

Please consider signing up for the GW-Project mailing list to stay informed about new book releases, events, and ways to participate in the GW-Project. When you sign up for our email list, it helps us build a global groundwater community. Sign up↗.

Cover Image: Example of time-lapse inversions showing the changes in bulk conductivity caused by the presence of amendment. After injection, the amendment experienced density-driven downward flow and lateral flow over the lower bounding unit contact at approximately 10 m depth. The progression from day 93 to day 371 shows the plume sinking and diluting.

Table of Contents

The Groundwater Project Foreword

The United Nations theme for World Water Day on March 22, 2022, is "Groundwater: making the invisible visible." This aligns with the essence of the Groundwater Project (GW-Project), which is aimed at raising groundwater consciousness and strengthening groundwater expertise worldwide, and is being accomplished by publishing books and supporting materials about "all-things-groundwater".

The GW-Project, a non-profit organization registered in Canada in 2019, is committed to contribute to advancement in education and brings a new approach to the creation and dissemination of knowledge for understanding and problem solving. The GW-Project operates the website https://gw-project.org↗ as a global platform for the democratization of groundwater knowledge and is founded on the principle that:

"Knowledge should be free and the best knowledge should be free knowledge." Anonymous

The mission of the GW-Project is to provide accessible, engaging, high-quality, educational materials, free-of-charge online in many languages, to all who want to learn about groundwater and understand how groundwater relates to and sustains ecological systems and humanity. This is a new type of global educational endeavor in that it is based on volunteerism of professionals from different disciplines and includes academics, consultants and retirees. The GW-Project involves many hundreds of volunteers associated with more than 200 organizations from over 14 countries and six continents, with growing participation.

The GW-Project, which began publishing books in August 2020, is an ongoing endeavor and will continue with hundreds of books being published online over the coming years, first in English and then in other languages, for downloading wherever the Internet is available. The GW-Project publications also include supporting materials such as videos, lectures, laboratory demonstrations, and learning tools in addition to providing, or linking to, public domain software for various groundwater applications supporting the educational process.

The GW-Project is a living entity, so subsequent editions of the books will be published from time to time. Users are invited to propose revisions.

We thank you for being part of the GW-Project community. We hope to hear from you about your experience with using the books and related materials. We welcome ideas and volunteers!

The GW-Project Steering Committee

November 2021

Foreword

When considered relative to the study of the atmosphere, rivers, lakes and oceans, the study of groundwater suffers from the disadvantage that groundwater is not visible. Boreholes are required to obtain direct measurements of groundwater systems, but boreholes are costly and disrupt subsurface conditions. Electrical imaging does not require drilling and provides insight about groundwater systems. This book describes that powerful geophysical method known as electrical imaging. It is founded on Ohm's Law in much the same way that understanding of groundwater flow is based on Darcy's Law. Darcy's Law concerns the resistance to water flow through permeable media whereas Ohm's Law involves the resistance of current flow through geological media. The aim of electrical imaging is to scan the subsurface by applying an electric current to the ground and monitoring voltage at many locations. Most often electrical imaging is employed to learn about the geology of a study area, although it can also be used to estimate depth to water or to find zones of saline water or oily industrial liquids. Learning about geology is essential to understanding a groundwater system. Drilled holes reveal the geology at each drill location but interpolation of the geology between holes is fraught with uncertainty. Electrical imaging can reduce the number of boreholes needed to characterize the subsurface or guide where boreholes can be most informative. Electrical imaging can also be used to monitor progress when liquids are injected into contaminated aquifers to remove or destroy the contaminants.

The ability of electrical imaging to provide valuable insight has increased markedly over the past few decades as technology for measurement of electrical responses and computing power for analyzing the responses have advanced with decreasing cost. Still, conversion of the data into meaningful information, requires careful design and analysis as well as consideration of multiple working hypotheses of subsurface conditions to best explain the electrical signals. This book enhances the reader's ability to use electrical imaging in understanding groundwater systems.

The authors of this book: Kamini Singha, a professor of hydrogeologic science at Colorado School of Mines; Timothy Johnson, a research geophysicist with Pacific Northwest National Laboratory; Frederick Day-Lewis, a chief geophysicist with Pacific Northwest National Laboratory, and Lee Slater, a professor of geophysics at Rutgers University, have many decades of cumulative experience with research, teaching and practice of electrical imaging. Herein, they explain, demonstrate and document best practices for collecting and analyzing electrical imaging data. They provide guidelines for those who decide to use this powerful geophysical method to reveal essential hydrogeologic information that is not feasibly obtained by other means.

<div align="right">

John Cherry, The Groundwater Project Leader

Guelph, Ontario, Canada, November 2021

</div>

Preface

Geophysical methods offer hydrogeologists unprecedented access to understanding subsurface parameters and processes. In this book, we outline the theory and application of electrical imaging methods, which inject current into the ground and measure the resultant potentials. These data are sensitive to rock type, grain size, porosity, pore fluid electrical conductivity, saturation, and temperature. Here we describe the physical basis for electrical imaging, parallels between electrical flow equations and the groundwater flow equation, practical considerations for field investigations, data processing and inverse modeling of field data, and how to QA/QC (Quality Assurance/Quality Control) data. We additionally cover two case studies, including a 2-D waterborne survey and a 4-D dataset from a biostimulation experiment.

Acknowledgements

We deeply appreciate the thorough and useful reviews of and contributions to this book by the following individuals:

1   Introduction

Electrical resistivity (ER, sometimes called ERI for electrical resistivity imaging or ERT for electrical resistivity tomography) is a direct-current (or low-frequency alternating-current) geophysical method that can be used to estimate the spatial and, in some applications, temporal distribution of subsurface *bulk electrical resistivity*, which describes the intrinsic resistance to electric current flow in geologic media. Bulk electrical resistivity, or its reciprocal, *bulk electrical conductivity*, is related to rock type, grain size, porosity, pore fluid electrical conductivity, saturation, and temperature; these relations underlie the utility of ER for cost-effective civil engineering and environmental studies, including imaging of lithology, differences in water saturation below ground surface, permafrost distribution, location of clays, and groundwater fluid conductivity, among other properties and processes as outlined in this book.

Although water in its pure state is non-conductive, the presence of dissolved salts in solution produces a conductive electrolyte to which ER methods are sensitive (e.g., Zohdy et al., 1974); hence, these techniques can be used to monitor multiple hydrogeologic processes such as infiltration, migration of ionic tracers or chemical amendments, and groundwater/surface water interactions. ER offers important benefits for hydrogeological studies: (1) many features, such as clay layers, variable moisture content, high salinity, low-porosity areas, and others, manifest as detectable electrical conductivity contrasts and vary in space; (2) instrumentation is relatively inexpensive, robust, and easy to operate; (3) instrumentation is mature and available commercially; and (4) ER measurements are amenable to automation, allowing for long-term, continuous, cost-effective monitoring.

Currently, while there are standards in terms of array types (Wenner, Schlumberger, dipole-dipole, as outlined in this book), there exist no community-accepted standards for ER survey design (i.e., which measurements are collected), quality assurance and quality control (QA/QC), or data analysis. In this book we review ER technology, the physics underlying ER measurements, and modeling and inversion approaches used in common ER software packages. We outline guidelines to ensure (1) design of robust survey geometries; (2) selection of appropriate acquisition and inversion parameters; and (3) documentation of data-collection configurations, QA/QC, and analysis procedures.

These practices are then demonstrated using a case study from the Defense Reutilization and Marketing Office (DRMO) Superfund site, in Brandywine, Maryland, USA (Johnson et al., 2014). Our objective is to document the best state-of-the-practice for an audience of hydrogeology students and practitioners while providing sufficient details on the mechanics of the method to relate the strengths and limitations of the data acquired. We refer more expert readers who are interested in advanced approaches to Johnson and others (2010), Singha and others (2014), or Binley and Slater (2020), all of which provide

valuable reviews of theory and applications of electrical imaging methods for a variety of systems.

Early ER field measurements relied on labor-intensive methods to build up information on the vertical (one dimensional, i.e., 1-D) variation of bulk electrical conductivity with depth or along a profile. The concept of modern electrical imaging was first described by Lytle and Dines (1978) and the first field demonstrations emerged in the 1990s (e.g., Griffiths et al., 1990). Over the last three decades, advances in ER hardware have resulted in multi-channel systems capable of controlling hundreds of electrodes and acquiring thousands of measurements per hour. During this same period, advances in software and computing power have led to the proliferation of user-friendly programs for ER *inverse modeling* (e.g., Cockett et al., 2015; Rucker et al., 2017; Blanchy et al., 2020) or, more simply, *inversion*, which refers to the mathematical process of estimating unknown subsurface parameter values from measured data. Inversion of three-dimensional (3-D) datasets through time, often called 4-D, is now becoming commonplace. Binley and Slater (2020) provide a recent review of ER methods that may be of interest to students moving beyond this text.

ER imaging suffers from several limitations that include: (1) the need for direct contact with the subsurface, which is problematic in areas with resistive surficial materials such as highways or permafrost (the exception is capacitively coupled systems for surface measurements, which do not require emplaced electrodes, but require resistive surficial materials and are not discussed here); (2) significant labor for electrode array deployment, particularly for long (many hundreds of meters) or 3-D arrays; (3) data collection can be slow and can limit monitoring of rapid dynamic processes depending on instrumentation and the number of electrodes; and (4) substantial user knowledge is required for processing of data, despite commercially available code (some options are listed in Section 4.1), if quantitative, rather than qualitative, interpretation of hydrogeologic processes is required.

Perhaps the biggest disadvantage is that, just like other geophysical techniques, we are dealing with proxies of what we want to actually measure. Bulk electrical conductivity has multiple dependencies that can complicate interpretation for a specific parameter or process. In addition, choices of regularization parameters and weighting the importance or accuracy of measurements may affect the magnitude and smoothness of ER estimates, further complicating quantitative conversion of electrical proxies to estimates of other physical properties (e.g., Day-Lewis et al., 2005). Collecting ER data through time, called *time-lapse imaging* as described in more detail throughout this book, is one way to alleviate this problem.

We also review an increasingly popular extension of ER in groundwater studies known as *induced polarization* (IP). This method measures transient voltages that result from temporary, reversible storage of electric current in the Earth—similar to the storage of water in aquifer systems as defined by storativity in the time-varying groundwater flow

equation—whereas ER is defined by a steady-state flow equation, as outlined below. The charge storage measured with IP primarily results from the electrical double layer forming at the mineral-fluid interface or at pore constrictions that locally reduce ionic mobility. IP measurements are consequently strongly sensitive to grain size, surface area, and pore size. When correctly acquired, the IP dataset provides valuable additional information that helps to constrain the hydrogeological interpretation of the subsurface relative to that possible from ER alone. This has important implications, including improved estimation of hydraulic conductivity from geophysical proxies (Slater, 2007). Most ER instruments allow an IP measurement to be made and most software for the interpretation of ER datasets supports the processing of IP measurements (if acquired) along with ER. Though IP is not commonly included in hydrogeologic studies because the time to collect IP data in the field is longer and processing and interpretation of ER and IP measurements combined requires additional expertise and understanding over that needed to use ER datasets effectively, as discussed in this book. Together, ER and IP comprise methods generally known as electrical imaging, which is the topic of this book.

1.1   Measurement Physics: The Relation between Data (Voltage Differences) and Parameters (Electrical Conductivity or Chargeability)

ER data acquisition systems drive an electric current that can range from milliamps (mA) to several amps into the subsurface through galvanic contact. Current is injected between two electrodes, a positive and a negative one (the *current electrodes*), and the resultant electric potential (specifically, the voltage difference) is measured between two or more additional electrodes (the *potential electrodes*, see Figure 1). The physics is mathematically analogous to a two-well pumping test, where water is injected in one well and removed from another, and the resultant head difference at steady-state would be measured between two other locations. This four-electrode injection/measurement procedure is repeated for as many combinations of current and potential electrode positions as desired, and usually involves the acquisition of many hundreds or thousands of multi-electrode combinations.
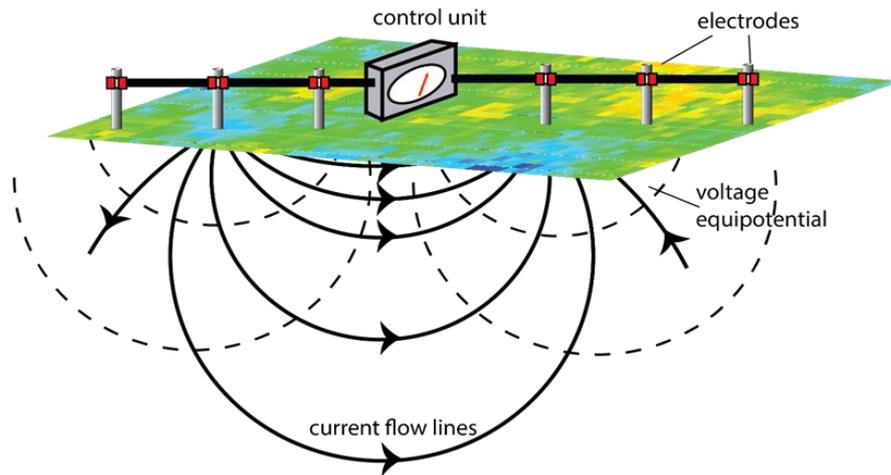
Figure 1 - Example of ER data collection. Multiple electrodes are installed along the ground surface (or in boreholes), and two electrodes at a time are used to drive current into the subsurface. The resulting voltage difference is measured between two or more potential electrodes. Flow and equipotential lines are analogous to those estimated from the groundwater flow equation, where current and fluid flux are mathematically parallel, as are voltages and heads, which are both potentials.

The measurements presented by ER instrumentation are voltage differences in volts (equivalent to differences in hydraulic heads in the analogy to groundwater flow), which are divided by the applied current to calculate *resistance* values (from Ohm's law, where $R = \Delta V/I$) in ohm (Ω), sometimes referred to as transfer resistance. The physical measurement of resistance is not an intrinsic property of a material (in our case rock or soil) because it depends on the geometry of, or distance between, electrodes used for measurement. A well-known example is the resistance of a length of wire. The resistance across 100 m of homogeneous copper wire would be 100 times the resistance across 1 m of the same wire. The wire has an intrinsic resistivity (in this case, the resistivity would be very low or the conductivity very high as copper is an excellent conductor) that limits current flow as evident from an observed voltage drop. Thus, in ER we measure a resistance that must be converted to a relevant intrinsic property, electrical resistivity, ρ (or its reciprocal, electrical conductivity, σ), from knowledge of the electrode locations. In the flow analogy, hydraulic conductivity is treated as an intrinsic property, whereas transmissivity is a function of geometry. In SI units, resistivity has units of ohm-meter (Ω-m) and conductivity has units of Siemens/meter (S/m). Each measured resistance is a function of the electrode locations, as noted above, and the electrical properties of both solids and liquids in the system.

The physics underlying ER measurements are described by the Poisson equation (Equation 1), which is a simplification of the Maxwell equations. This is also the equation that describes steady-state groundwater flow.

$$\nabla \cdot \sigma(x,y,z)\nabla V(x,y,z) = -I\delta(x - x_s, y - y_s, z - z_s) \tag{1}$$

4

subject to boundary conditions, where:

∇ = gradient operator

$\nabla \cdot$ = divergence operator

σ = electrical conductivity, an intrinsic property of the material (Siemens/meter)

V = electric potential (Volts), where V can be used to determine the voltage differences between two potential electrodes for a given current injection

I = electric current source magnitude, otherwise known as the current injected in the field (Amperes)

δ = Dirac delta function

x, y, z = spatial position vectors (meters)

x_s, y_s, z_s = spatial coordinates of the current source (meters)

As with the groundwater flow equation, Equation 1 can be simplified to an equation for two-dimensional (2-D) systems, and/or to an equation where the electrical conductivity is considered to be homogeneous and isotropic (see Section 7 of the Groundwater Project book "Hydrogeologic Properties of Earth Materials and Principles of Groundwater Flow"↗). 3-D data acquisition and inversion methods are increasingly practical and appropriate, although many practitioners still use 2-D inversion. Commonly, commercially available software for 2-D inversion invokes what is known as a *2.5-D assumption* for computational efficiency. Under this assumption, inverse modeling is performed for a 2-D parameterization (e.g., to identify the best-fit cross section), while forward modeling of the electrical measurements is performed in 3-D. The 2-D structure is assumed to extend infinitely into the third dimension (e.g., Dey and Morrison, 1979; LaBrecque et al., 1996; see Section 0.2 for more details). The 2.5-D approximation thus combines a 2-D parameterization with 3-D physics. Conceptually this is similar to classical pumping test analysis, where hydrogeologists combine a 1-D parameterization (layers) and 2-D (axisymmetric) flow.

Equation 1 combines conservation of charge and *Ohm's law*. Ohm's law, shown in continuous form by Equation 2, is the constitutive relation analogous to Darcy's law, linking electrical (as opposed to hydraulic) potential gradients and fluxes.

$$j = -\sigma \nabla V \tag{2}$$

In geophysics, this link is assumed to be linear. Here, j is the electric current density (*Amperes/m^2*) in the ground in response to the external current source (I) and is analogous to the specific discharge in Darcy's Law. In adopting Equation 1, we make some important assumptions about our measurement. Equation 1 assumes equilibrium or steady-state electrical conditions and includes neither transient (i.e., induced polarization) effects nor current sources other than what is injected through the current electrodes (e.g., no spontaneous potentials), which are assumed to act at a single point (i.e., x_s, y_s, z_s). The

5

validity of these assumptions depends in part on instrument settings, as explained in Section 0, below. Equations 1 and 2 describe the link between the subsurface potential distribution (*V*), which determines the voltage differences between two potential electrodes (Δ*V*), the current injection magnitude and location, and the electrical conductivity (*σ*).

In some software packages, the data are specified in terms of resistance (Δ*V/I*) where both *I* and Δ*V* are reported by the instrumentation. Other packages expect data in the form of *apparent resistivity*, ρ_a, which is the resistivity that the subsurface would have if it were homogeneous and isotropic and is calculated as shown in Equation 3.

$$\rho_a = K_g \, (\Delta V/I) \tag{3}$$

K_g is a *geometric factor* (in meters) accounting for electrode configuration. In our earlier example of the copper wire, this geometric factor is simply the cross-sectional area of the wire divided by its length. Apparent resistivity is sometimes preferred over resistance because it scales the data to have the same units and magnitude as the intrinsic property being estimated (electrical resistivity), and thus it is more intuitive. Note that the resistance measurements can be both positive and negative, as geometric factors can be positive or negative. It is important to note that intrinsic subsurface electrical conductivity cannot be negative, and neither are the magnitudes of injected currents. However, the sign of the measured potential difference is purely dependent on which electrode we use as our reference electrode, and thus negative voltages (and resistances) can be recorded. Although the apparent resistivity is typically positive, negative apparent resistivities are also possible. A measurement that would be positive under homogeneous subsurface conditions may be negative under certain heterogeneous subsurface conditions (e.g., Wilkinson et al., 2008; Jung et al., 2009). For this reason, it is crucial to collect *signed voltage differences* in the field, rather than the absolute value of the voltage difference between electrodes. The use of apparent resistivity can be helpful in assessing measurement errors when compared to examining resistance values, given that the apparent resistivity values are of similar magnitude to one another. In the field, geophysicists used to plot *pseudosections* of apparent resistivity, which assign the volumetric measurements to a point location in *x-z* space based on the measurement-electrode locations (e.g., Hallof, 1957); these plots are still generated by many inversion programs. In general, plotting measurements prior to inversion is important for visualizing trends that may be indicative of certain subsurface objects or to identify obvious errors as in the case of malfunctioning electrodes.

Induced polarization measurements record the effect of temporary charge storage on the electric field. One way to observe storage effects is to capture the transient voltage decay that occurs on abrupt termination of the applied electric current when the Earth stores charge. This *time-domain IP effect* is quantified as an integral of V_m, the voltage decay

curve, from t_1 to t_2 divided by the primary or total voltage (V_T) as shown by Equation 4 and in Figure 2a.

$$M_a = \frac{1}{(t_2 - t_1)} \frac{\int_{t_1}^{t_2} V_m}{V_T} \tag{4}$$

M_a is the apparent chargeability. Similar to apparent resistivity, the *apparent chargeability* depends on the electrode locations and is different from the *intrinsic chargeability* of the subsurface, which describes the polarization strength of a geologic material. It is worth noting also that sampling period is not standard between different instruments and may affect measurements; thus, instrument settings must be consistent to allow for meaningful comparisons of measurements between surveys. A number of conventions have been proposed, e.g., integration over one log cycle or a specified time window (Sumner, 1976). Apparent and intrinsic chargeability are both unitless although typically expressed as *mV/V*.
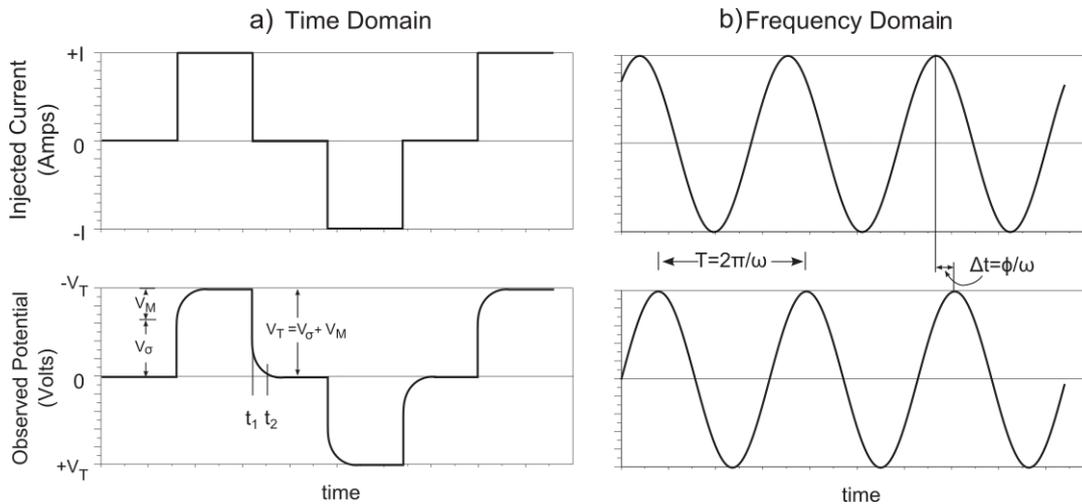
Figure 2 - Different ways to measure induced polarization: a) a time-domain measurement, where voltage decay is recorded following abrupt current termination, and b) a frequency-domain measurement, where magnitude and phase of a sinusoidal voltage with a period T (related to frequency ω recorded between two electrodes lags behind the current recorded across a reference resistor placed in series with the Earth by a time Δt. Note that in ER measurements, voltages are only measured at the plateau of the injected current (i.e., V_T), not during the decay.

The intrinsic chargeability or phase of the Earth must be positive. However, the measured apparent chargeability or measured apparent phase over a heterogenous Earth can be positive or negative, depending on the location of chargeable objects relative to the sensitivity pattern of the electrode array, described in more detail below. Any array will have some regions of *negative sensitivity*, where in ER, an increase in subsurface resistivity will counterintuitively be observed as a decrease in measured resistance. When a highly chargeable object is located within this region of negative sensitivity, a negative apparent chargeability can be recorded with IP (Dahlin and Loke, 2015). When expressed with respect to a complex impedance or complex resistivity, the phase should normally be negative, being consistent with Figure 2 where the voltage lags in time behind the current

7

The GROUNDWATER PROJECT   ©The Authors   Free download from gw-project.org

Anyone may use and share gw-project.org links. Direct distribution of the book is strictly prohibited.

waveform. However, the measured apparent phase recorded over a heterogeneous Earth can sometimes be positive (Luo and Zhang, 1998; Wang et al., 2020) as a result of the sensitivity patterns of an array. A practitioner may be tempted to discard negative apparent chargeabilities or positive (for complex impedance or resistivity) apparent phase as data errors. Error checks, described in Section 3.3, can help to differentiate between errors and negative apparent chargeabilities that inform on the subsurface structure.

The physics of induced polarization can be incorporated into Equation 1 by representing the conductivity and potential gradient terms as complex numbers, as shown in Equation 5.

$$\nabla \cdot \sigma^*(x, y, z)\nabla V^*(x, y, z) = -I\delta(x - x_s, y - y_s, z - z_s) \tag{5}$$

Here, σ^* is known as the *complex conductivity*. The real and imaginary components of the complex conductivity separate out the electrical conduction and polarization properties of the subsurface. In the mathematical analogy to groundwater flow, chargeability is related to parameters controlling storage (e.g., specific storage or storativity), and Equation 5 resembles the transient groundwater flow equation with a single complex-valued parameter, σ^*, where the real part relates to resistance (or its reciprocal, conductance) and the imaginary part to reactance (or its reciprocal, susceptance). Indeed, the electrical analogy for the transient problem was the basis for simulating non-equilibrium groundwater flow using resistor-capacitor networks prior to the advent of digital computing (Freeze and Cherry, 1979).

Frequency-domain IP considers measurements in terms of the frequency of waveforms (Figure 2b), which are made by using a sine-wave current source, and measuring the *magnitude* and *phase* ($\varnothing$) of the *complex resistance* $(\Delta V/I)^*$ or of the *complex apparent resistivity* ρ_a^*. The phase refers to the phase shift between the injected current and the measured voltage and is the frequency-domain measure of the *IP effect*. In the absence of current storage (either in non-polarizing materials or because we do not measure the time-varying piece), $\varnothing = 0$ and Equation 5 simplifies to Equation 1. Frequency-domain measurements are popular in the laboratory, and some instruments exist to perform field-scale frequency-domain acquisition. However, it is often simpler to measure the field IP effect using *time-domain IP* (Figure 2a). The time-domain and frequency-domain IP effects are theoretically equivalent, and one can be determined from the other through a Fourier transformation (the Fourier transform of a time series is a complex valued function of frequency).

Regardless of whether IP data are being collected, the goal of data collection is to create a cross section or volume distribution of subsurface electrical conductivity in *x-y* (or *x-y-z*) space, which requires the process of inversion, described in detail in Section 0. Inversion software solves the *forward model* problem using Equation 1 or 5, which takes assumed model parameters (electrical conductivity or resistivity and chargeability or

phase) and produces model predictions that can be compared with observed data—resistances or apparent resistivity and apparent chargeability or apparent phase. ER inversion is commonly done using finite-difference or finite-element techniques for solving partial differential equations, where Equation 1 (or Equation 5 in the case of IP) is solved at spatially distributed discrete locations corresponding to the centers of finite-difference grid cells or to nodes in a finite-element mesh, with the accuracy of the solution depending on the level of discretization, as outlined in Section 2.2. Finite-difference codes are not frequently seen for surface data collection due to complexities with topography. Depending on the survey geometry (i.e., number and placement of electrodes), inversion can produce 1-, 2- or 3-D *tomograms*, reconstructed images that show the estimated subsurface distribution of electrical resistivity or conductivity. The term *tomography* refers to the image reconstruction process using ER measurements and is described in Section 0.

1.2   Electrical Imaging Hardware and Field Deployments

To inject electric current and collect the requisite resistance measurements in the field (Figure 3), a series of electrodes are attached to an ER control unit, which consists of a regulated current source (for example, a 12-V deep-cycle battery or a generator), voltage meter, current meter, and *multiplexers* (units for switching between electrodes) for multi-channel data collection. Despite the advent of *multi-node cables* (i.e., cables with connection points, called *takeouts*, for many tens of electrodes, as shown in Figure 3), considerable labor is still required for the initial deployment of cables. However, once the instrumentation deployment is complete, it can be left in place for many hours to years to explore changes in electrical conductivity through time associated with processes, which is a reason these methods show strength for time-lapse monitoring. Commercially available multi-channel electrical imaging systems commonly accept input files listing the selected four-electrode current-potential pairs, called *quadripoles*. These files are variously referred to as *sequence*, *command*, or *schedule* files. The control unit then drives current on two electrodes and measures potential differences between two or more electrodes based on the input sequence file.
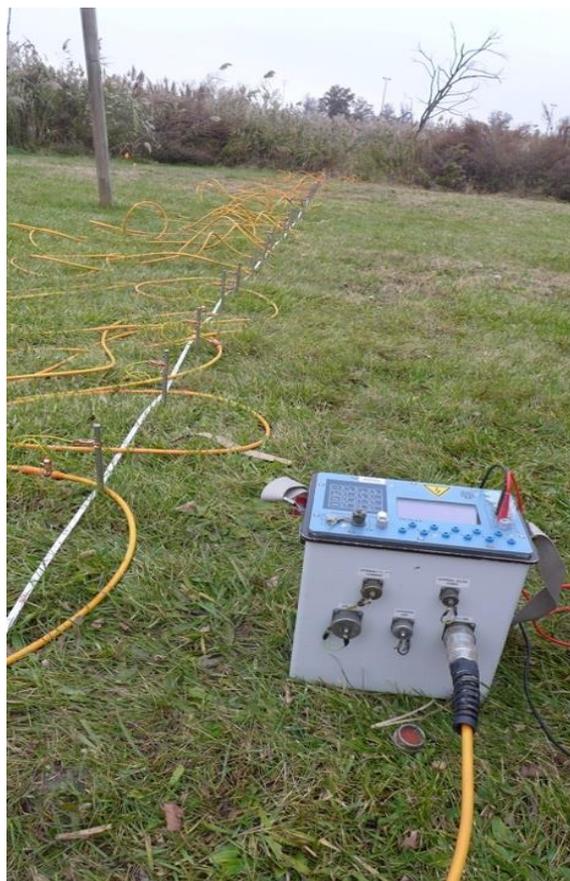
Figure 3 - Electrical imaging instrumentation, including the control unit in the foreground, electrodes, and cables that connect the control unit to the electrodes. The batteries and multiplexers are inside of this control unit. From Binley and Slater (2020).

Commercial systems on the market today generally are constant-voltage systems, i.e., they establish a constant voltage difference over the current electrodes and measure the resulting current. Thus, the amount of current driven is influenced by the conductivity of the Earth, where lower input currents may be needed in resistive settings where potential differences are larger, and higher input current is needed in conductive settings. Typical currents are usually in the mA to A range. Subsequent measured voltages are usually in the μV to V range. Electrodes are commonly composed of stainless steel or graphite. Steel electrodes tend to be more durable, whereas graphite electrodes resist corrosion and thus are preferred in marine deployments. In applications where *spontaneous potential* (SP) data (based on naturally occurring voltages in the earth) are collected in addition to ER, non-polarizing electrodes (e.g., copper/copper-sulfate) are necessary for making voltage measurements. For a review on various electrode types, see Morris and others (2004) and LaBrecque and Daily (2008). SP is beyond the scope of this book, but it is worth noting that SP data are complementary to ER and IP data, can help to reduce uncertainty in interpretation of hydrogeologic systems, and can be used to interpret flow directions in some applications.

10

IP data acquisition uses the same hardware as ER, but additional considerations are needed to acquire reliable measurements. Any hydrogeologist considering the use of IP should be aware that it is substantially more challenging than ER surveying alone, and more time consuming to collect in the field. This is because the signal-to-noise ratio of the IP measurements ($\emptyset$, M_a) is typically 2.5 to 3 orders of magnitude smaller than the magnitude of the resistance recorded with ER, and accurate transmitter-receiver synchronization is needed. In addition, *electromagnetic and capacitive coupling* between the different wires used to connect the current injection and voltage recording electrodes is manifest as spurious charge storage effects that may corrupt the response from the earth. Field procedures have been developed to alleviate these concerns, including separating the wires that connect to the voltage-receiving pairs from those that connect to the current-injection pairs (e.g., Dahlin and Leroux, 2012).

Regardless of the type of electrode used or whether ER or ER and IP data are being collected, it is important to record locations of the electrodes accurately in the field, as well as electrode and transect elevations, which will be incorporated into the inversion procedure to get the correct topography for the upper boundary (see Section 3.6). The accuracy required for surveying and georeferencing of electrodes is highly dependent on the survey design, with greater accuracy required for smaller electrode spacing or in areas of more topographic relief.

2　Designing Surveys

ER and IP data can be collected on the earth surface—including in water bodies, in boreholes, or both. The volume of subsurface sampled, sometimes called the *depth or distance of penetration* of the current, depends on the (unknown) electrical conductivity structure of the subsurface and the spacing of the electrodes and is, therefore, difficult to quantify or predict prior to data collection and analysis (e.g., Daily and Ramirez, 1995), which partially accounts for variable practices of data collection. Many surface studies successfully image electrical conductivity to depths of a few tens of meters below ground surface. The depth to which a particular survey can image effectively depends on the survey geometry, measurement errors, and the subsurface conductivity structure. The depth of penetration can be interpreted from sensitivity or resolution maps (e.g., Figure 4), or Oldenburg and Li (1999) provided an inversion-based approach (see more on inversion in Section 0) to predicting what they instead termed the *depth of investigation* (DOI). For DOI calculations, two inversions are performed using two reference models which differ by orders of magnitude, and the resulting images are compared. Depending on the type of regularization used (see Section 0.2 for definitions and details), the images are either differenced or cross-correlated to determine the depth to which the inversion is strongly affected by the reference models, i.e., below this DOI the data provide negligible information. This approach is supported in some inversion software. Simpler approaches to predicting DOI (e.g., Barker, 1989) are based on calculating the measured signal versus depth for a homogeneous half space and identifying the depth corresponding to the maximum, mean, or median signal contribution. These approaches produce simple rules of thumb for various array types and provide practical guidance for survey design. For example, for the popular dipole-dipole array, the median depth of investigation is on the order of 1/5 the maximum electrode spacing in an array (Roy and Apparao, 1971). The important messages here are 1) that some parts of the tomogram will be better resolved than others; 2) there are multiple tools to assess where resolution is expected to be high, and these methods are not absolute measures of accuracy; and 3) there is limit to how far from the electrodes ER and IP can see, which is impossible to determine in advance as it is dependent on the electrical conductivity of the earth and the geometry used to collect data, described below.
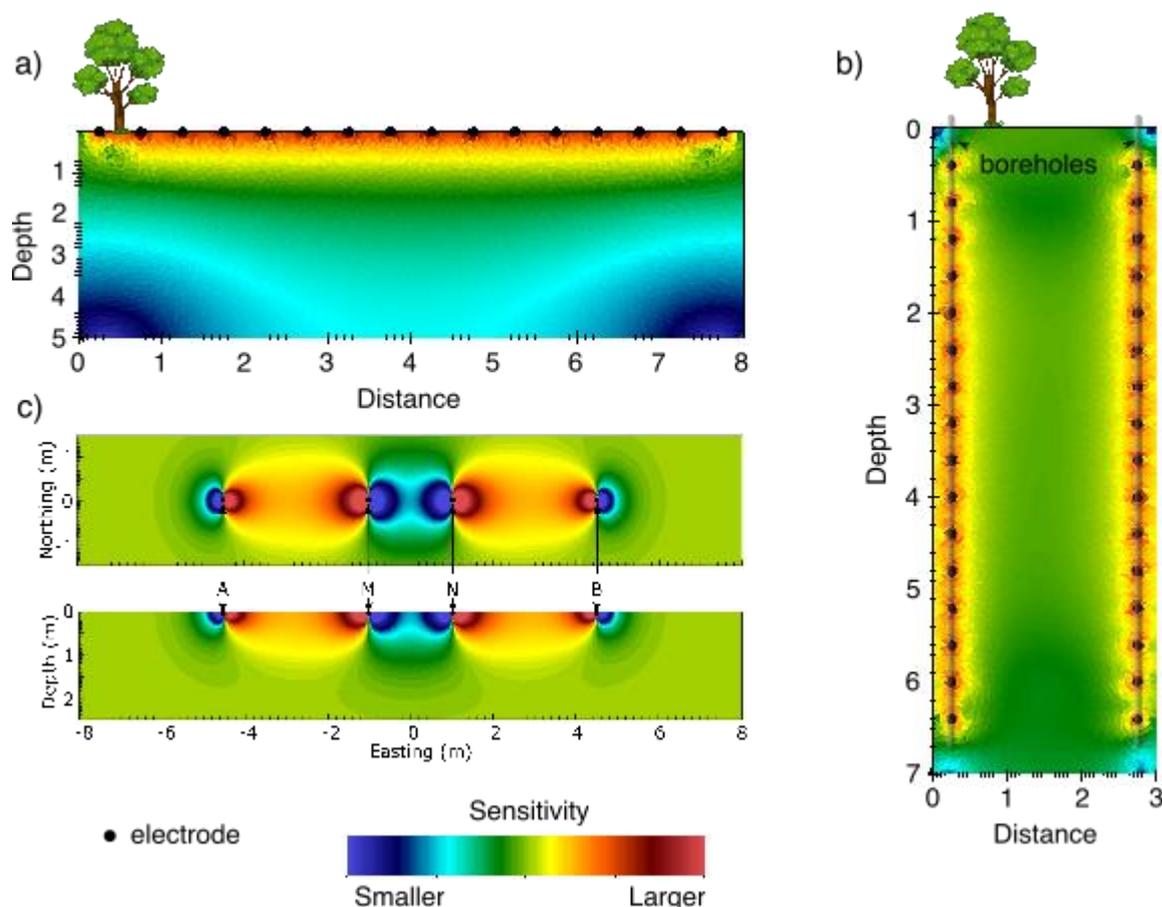
Figure 4 - Cumulative squared sensitivity maps (a proxy for resolution) for surface a) and crosswell b) ERT arrays. These maps are the sum of squared sensitivity (the diagonal of J^*J') where J is the Jacobian matrix and J' is its transpose. The Jacobian matrix is a matrix of first-order partial derivatives that shows the sensitivity of the model parameters to the data (more details in Section 4.2). c) The absolute sensitivity for a single measurement (i.e., a single row of J); cool colors are negative sensitivity and warm colors are positive (on c only).

Sensitivity is generally highest near the electrodes (Figure 4), whether the electrodes are on the surface or in boreholes. Practitioners are faced with a tradeoff between resolution and spatial coverage. Resolution improves with smaller electrode spacing, but smaller spacing (or well offsets) for a fixed number of electrodes reduces the volume of the subsurface studied. Consequently, when designing a survey, it is important to keep in mind the depth and size of targets. In field surveys and in the presence of heterogeneity, the volume of earth sampled by a particular resistance measurement is unknown—not unlike estimating the volume of earth sampled by a pumping test—and conversion from resistance to electrical conductivity requires inverse modeling. Information on inversion and image reconstruction is outlined in Section 0.

Historically, ER and IP data were collected on the surface using a fixed set of electrode geometries where the two current and two potential electrodes were moved by hand. However, such fieldwork was highly labor intensive. Modern systems are almost always automated using tens to hundreds of electrodes in an array. Some standard array types are often used in the field, such as Wenner, dipole-dipole, or Schlumberger arrays

13

The GROUNDWATER PROJECT   ©The Authors   Free download from gw-project.org

Anyone may use and share gw-project.org links. Direct distribution of the book is strictly prohibited.

(Figure 5). Some geometries (e.g., Wenner) are favored for their sensitivity to vertical contrasts in electrical conductivity, whereas other geometries (e.g., dipole-dipole) are favored for sensitivity to lateral changes in electrical conductivity. IP measurements benefit from arrays where the voltage pair are nested between the current pair, as with the Wenner and Schlumberger arrays, because of their high signal-to-noise ratio, although this comes at the expense of additional electromagnetic coupling effects relative to non-nested arrays such as dipole-dipole. By restricting data collection to simple geometries, analytic methods could be used to estimate the subsurface electrical conductivity without numerical modeling and inversion (for example, Zohdy et al., 1974). While selection of an ideal geometry has been the subject of past research, the ability to resolve subsurface structure is dependent not only on the geometry used, but on the electrical-conductivity structure of the subsurface, which is unknown. Optimized sets of measurements based on arbitrary array geometries can now be designed based on considerations of the expected subsurface structure (e.g., Stummer et al., 2004). Modern inversion software is capable of processing ER and IP data in minutes on a low-end PC and does not require that the electrode arrangement corresponds to any of the traditional, standard array types.
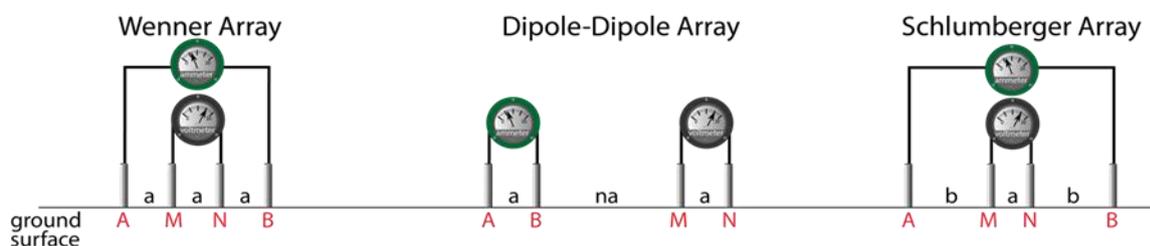
Figure 5 - Some common surface electrode geometries for ER and IP, including Wenner, dipole-dipole, and Schlumberger arrays, which have different positioning of current (A,B) and potential (M,N) electrodes, as defined by spacings a and b and n, an integer.

For n electrodes, the number of fully independent 4-electrode measurements (i.e., quadripoles) is $n(n\text{-}3)/2$ (Xu and Noel, 1993). Collecting all possible combinations of measurements is often unrealistic in the field given the memory constraints of ER meters and the time required to collect the data. Depending on the speed of data acquisition (i.e., instrument capabilities and measurement times) and whether time-lapse data are required (which may constrain the time allowed for measurements), an appropriate number of quadripoles can be selected. The choice of which quadripoles to collect in the field can be determined by two criteria: (1) geometric factors and (2) signal-to-noise ratios (dependent on the site). Larger electrode spacings will require larger source voltages to get sufficient current into the ground to ensure good data quality. Injected current is limited by the equipment and the resistivity of the ground. With respect to the speed of data collection, new *multi-channel* instrumentation, capable of multiple voltage measurements at once for a given current pair—one voltage measurement at a time per channel—leads to faster data collection than older single-channel tools, although this functionality may only be applicable for certain array types depending on the instrument. To fully capitalize on

14

multi-channel data acquisition, surveys can be designed to minimize the number of unique current injections collected during a given survey.

In borehole surveys, selected quadripoles would ideally combine in-well and cross-well dipoles, i.e., with current pair in one well and potential pair in a second, as well as with current and (or) potential pairs split between wells. In-well dipoles are sensitive to targets located near boreholes, but do not provide much information farther from boreholes. Cross-well dipoles are more sensitive to targets located farther from wells. To collect quality cross-well data, the boreholes should be approximately at least 1.5 times as deep as they are far apart. For much larger offsets, resolution between boreholes becomes highly degraded.

2.1   Geometric Factors

We introduced the concept of the geometric factor (Equation 3) as the parameter that converts a measured resistance to apparent resistivity. For surface arrays, the underlying math to calculate the geometric factor is fairly simple. Assuming a homogeneous and isotropic *half space* (meaning the same electrical conductivity in the earth to infinite distance below a surface boundary) without any electrical sources, the geometric factor K_g for every quadripole can be calculated for surface arrays using Equation 6a.

$$K_g = \frac{2\pi}{\frac{1}{\overline{AM}} - \frac{1}{\overline{AN}} - \frac{1}{\overline{BM}} + \frac{1}{\overline{BN}}} \tag{6a}$$

$\overline{AM}$, $\overline{AN}$, $\overline{BM}$, and $\overline{BN}$ are the distances between electrodes A and M, A and N, B and M, and B and N, respectively. Current electrodes are defined as A and B and potential electrodes are M and N. Current electrodes are defined as A and B and potential electrodes are M and N (Figure 5). These electrodes are often also called $C+$, $C-$, $P+$, and $P-$, respectively, in other literature, however the older A, B, M, N standard is used in this book. The geometric factor accounts for the arrangement of electrodes and allows one to calculate an apparent resistivity (Equation 3).

For borehole geometries, the electrodes are located within the half-space rather than at the boundary at the Earth's surface. In this case, use of Equation 6a is inappropriate, as it does not account for the no-flow boundary at Earth's surface. To account for the effect of the boundary on cross-well measurements, the *method of images* from optics is invoked. This approach is analogous to the use of image wells in groundwater hydrology for analytical modeling of aquifer response to pumping. Here, imaginary *image current electrodes* are introduced on the other side of the boundary, equidistant from the real current electrodes, to mathematically produce a no-flow condition at the Earth's surface and calculate a geometric factor for borehole arrays as shown in Equation 6b.

$$K_g = \frac{4\pi}{\frac{1}{\overline{AM}} + \frac{1}{\overline{A_{image}M}} - \frac{1}{\overline{AN}} - \frac{1}{\overline{A_{image}N}} - \frac{1}{\overline{BM}} - \frac{1}{\overline{B_{image}M}} + \frac{1}{\overline{BN}} + \frac{1}{\overline{B_{image}N}}} \tag{6b}$$

Here, "*image*" indicates the image current electrode. When the electrodes are all on the boundary, Equation 6b simplifies to Equation 6a. Also, limited burial is necessary before Equation 6b simplifies to twice the result of Equation 6a, as the distances from the potential electrodes to the true current electrodes and their images are approximately equal.

Quadripoles with large geometric factors may produce small voltage differences, which are prone to measurement errors due to a lower signal-to-noise ratio. These are manifest (via propagation of errors) as higher relative errors in apparent resistivity data. A critical geometric-factor cutoff can be determined based on the average expected electrical conductivity of the subsurface and the instrument specifications. Based on Equation 3, for a given geometric factor and expected instrument error (in terms of voltage, inserted as the potential difference), we can calculate the expected error in apparent resistivity. Figure 6 illustrates how error in measured potential difference translates into error in calculated apparent resistivity as a function of K_g. In this example, we consider an applied current of 50 mA and assume a 1-microvolt *(μV)* instrument accuracy (note the logarithmic scale). In practice, accuracy may be less. As evident in Figure 6, for large geometric factors or small assumed apparent resistivity, errors are larger relative to measurements.
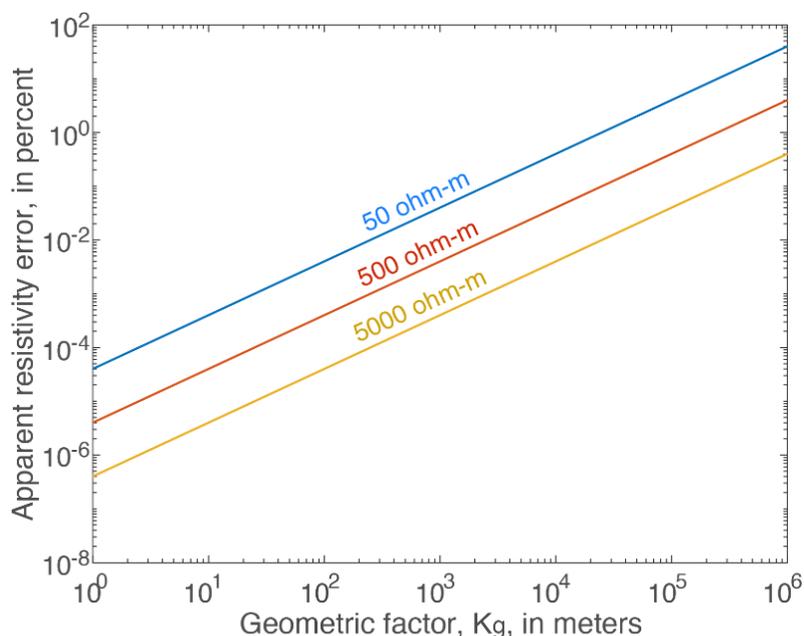
Figure 6 - Apparent resistivity error, as a percentage of the true apparent resistivity, as a function of geometric factor for three different values of resistivity (50, 500, and 5,000 Ω-m), assuming the voltage accuracy is 1 microvolt and the applied current is 50 milliamperes, where apparent resistivity error is given by K_g*V_{error}/I, which is then compared to the assumed apparent resistivity in a relative sense. An error in the measured voltage translates into error in calculated apparent resistivity as a function of K_g. In practice, larger errors may occur in the field.

2.2   Synthetic Models

Forward modeling is a powerful tool in the design and simulation of electrical imaging surveys. Forward modeling codes are commonly based on finite-difference or finite-element solutions of the Poisson equation (Equation 1 for ER only and Equation 5 for ER and IP). Forward-modeling codes can simulate "synthetic data" for different spatial distributions of electrical conductivity (and phase or intrinsic chargeability for IP), survey geometries, and random noise levels for a given discretization of Equation 1 or 5 (Figure 7a). Common software packages allow users to set the size of finite-difference cells or finite elements. These predicted data can be inverted to generate tomograms (Figure 7b and Section 0). Such exercises provide insight into the resolving power of different survey geometries, noise levels, and inversion approaches.
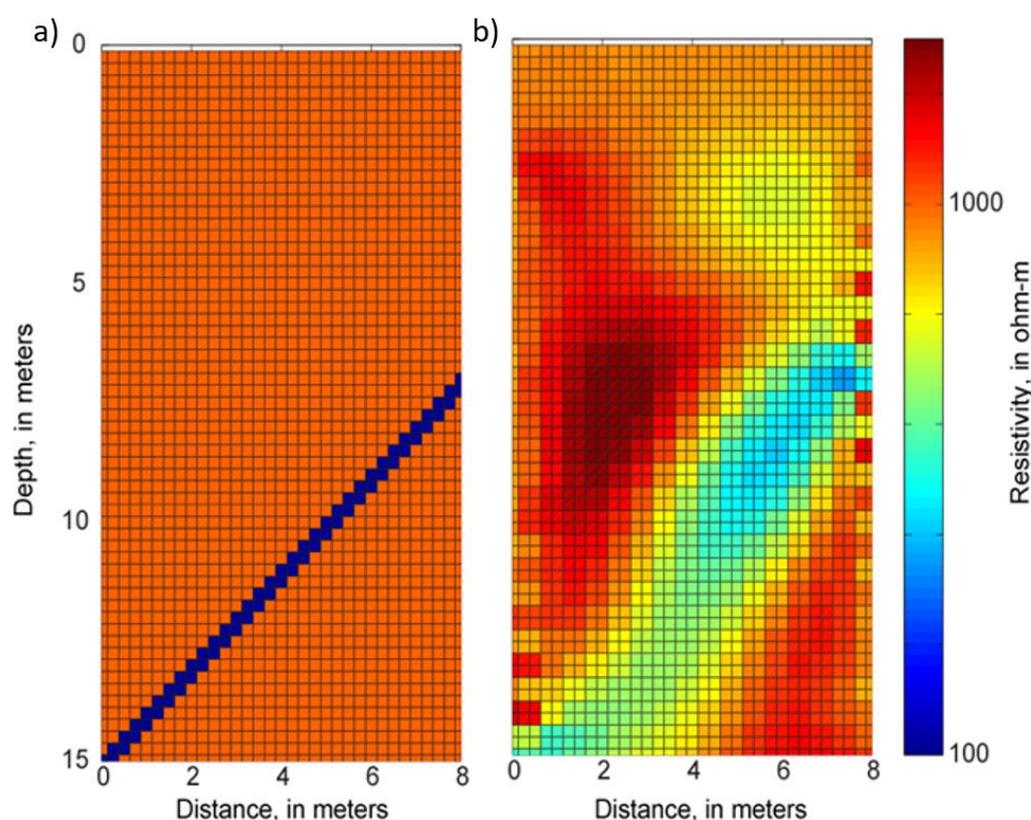
Figure 7 – a) Hypothetical electrical resistivity cross section, and b) resulting tomogram. Because of the limited resolution of the survey and regularization in the inversion routine, the tomogram is a blurred, blunted version of reality.

Forward-model accuracy is thus another factor to consider in designing survey geometries. We should eliminate quadripoles that are expected to have large modeling errors from our measurement sequence. We can quantitatively evaluate the forward-model accuracy by modeling the apparent resistivity for all candidate quadripoles assuming a homogeneous Earth (i.e., a single conductivity) and comparing them to the apparent resistivities based on the geometric factors calculated analytically above. Quadripoles that do not model well (i.e., the apparent resistivity calculated numerically differs substantially

17

from that computed analytically) should not be collected in the field, or the discretization of the mesh and the location of the boundary conditions should be refined if problems exist or too many data are eliminated in this manner. This exercise can only be performed in the simple case where an analytical solution to Equation 1 exists. For example, in the presence of a heterogenous subsurface or topography, analytical solutions are not generally available, and assessment of numerical model accuracy is cumbersome for thousands of quadripoles. Hence test criteria are based on simple analytical models, assumptions of homogeneity, or criteria based on experience. As a rule of thumb, grid spacing near electrodes where potential gradients are large should be finer than one quarter of the electrode spacing. Grid spacing can be coarser further from electrodes where voltage gradients are smaller. Commonly, grid spacing is increased by a factor of less than 1.5 from one grid row or column to the next, deeper or neighboring row in finite-difference models. In finite-element models, unstructured meshes are typically refined about the electrodes with similar discretization.

In the example of Figure 7, a cross-well ER survey is conducted for a cross section containing a single 25-cm fracture zone and no other heterogeneity. Assuming a low-noise dataset, 2 percent random, normally distributed errors are added to the data to introduce noise as might be expected in the field. The resulting tomogram provides only a blurry and blunted image of the true electrical conductivity distribution, and interpretation of the location and extent of the fracture zone is complicated by the limited resolution. If another heterogeneity existed in the cross section (for example, lithologic or porosity variation), or if the fracture zone was a small discrete fracture (perhaps 2.5 mm instead of 25 cm), it might not be possible to identify the fracture at all. By considering different input models, or targets, it is also possible to gain insight into how resolution varies spatially over a tomogram. Indeed, conducting such *synthetic modeling* exercises prior to field surveys represents a best practice. Many ER modeling and inversion software packages can be used for this purpose. Open-source and free solutions for testing scenarios include:

- the United States Geological Survey spreadsheet-based Scenario Evaluator for Electrical Resistivity (SEER), which approximates the inversion of ER data and is particularly aimed at the non-expert (see Figure 8 and also Terry et al., 2017); and,
- ResIPy (Blanchy et al., 2020), an intuitive graphical user interface for the family of ER and IP inversion codes written by Andrew Binley (Lancaster University).
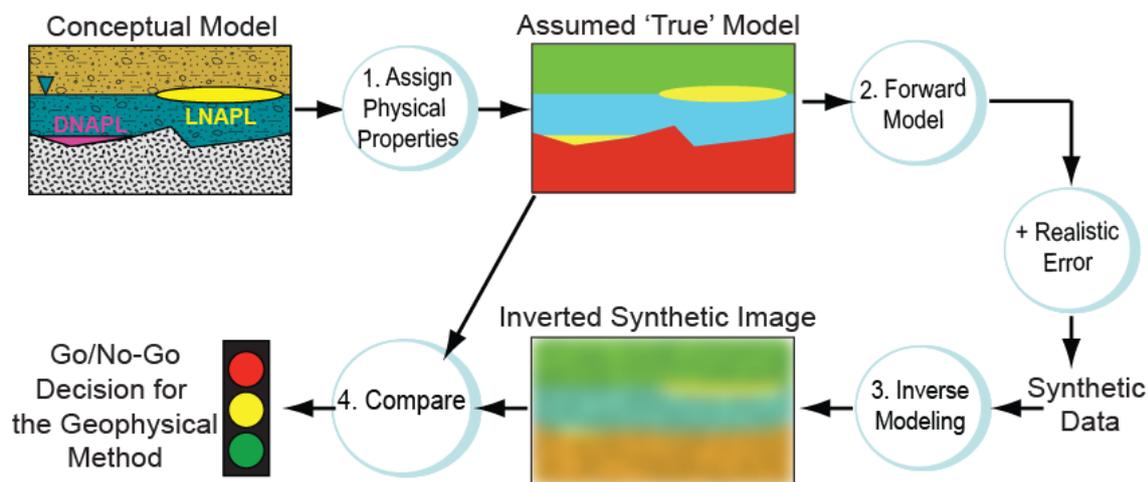
Figure 8 – Synthetic modeling workflow. The steps are: 1) assign best-guess physical properties for the hypothetical subsurface model; 2) forward model, i.e., calculate the data that would result from the assumed 'true' model entered by the user in the first step and corrupt the data with random errors for realism, generating 'synthetic data'; 3) analyze the synthetic data by inverse modeling to produce an image, or tomogram; and 4) compare the inverted synthetic image with the assumed true model. If the synthetic image does not sufficiently resolve the target sought, i.e., a light non-aqueous phase liquid plume in this schematic, field implementation of the method will likely fail and should be discouraged. After Day-Lewis and others (2017) and Terry and others (2017).

Box 1↴ of this book provides an opportunity for readers to experiment with the electrical resistivity modeling software SEER and explore the impact of some survey design parameters on the resulting electrical image.

3   Collection and Verification of Field Data

In addition to quadripoles collected, it is highly advisable to collect (1) electrode contact resistance measurements, (2) stacked or repeated measurements, and (3) reciprocal measurements. As described below, these measurements allow the user to evaluate the quality of the data both in the field and later during analysis back in the office. Accurate assessment of measurement errors is often critical for obtaining an optimal image from the inversion procedure.

3.1   Contact Resistance

Contact resistance refers to the resistance to current flow between the current electrodes and the surrounding medium (soil, water, rock). Recorded contact resistances are the sum of the resistances of the contacts between each current electrode and the ground and the resistance of the formation between the current electrodes. Resistance checks should be run on the electrodes prior to data collection to assure that contact resistances are not too large. This test is the key quality control in the field. Cutoffs on the order of tens of kiloohm (kΩ) may help determine where limited current will be injected for an electrode pair. It is difficult to come up with absolute numbers for this metric because contact resistance measurements vary with geology. For example, crystalline rock may have high contact resistance measurements due to the formation resistivity, but quality data are still possible to collect. Contact resistances should be recorded manually if not automatically recorded by the instrument software. Contact resistance measurements commonly can be made automatically with modern ER instrumentation, which applies a small voltage to the current injection electrodes, measures the resulting current with the ER instrumentation, and computes the resistance by dividing the applied voltage by the injected current. Alternatively, manual contact resistance measurements for a given electrode pair can be made with a voltmeter by measuring the resistance between corresponding pins in the head of the electrode cable. Contact resistance values can provide a basis for editing data associated with particular electrodes that exhibit poor contact with the formation, allowing corrections to be made prior to a survey. Low-contact resistances are critically important for the collection of reliable IP datasets because the signal-to-noise ratio of IP measurements is typically 2.5 to 3 orders of magnitude smaller than resistance measurements. In fact, contact resistance is often the limiting factor preventing acquisition of meaningful IP data (Zarif et al., 2017), as is also true for ER. For more advanced reading on contact resistances, we point readers to the 2013 paper by Hördt and others.

In surface arrays, it is possible to add a small amount of saltwater around electrodes to improve contact resistance, but this generally is not possible for cross-well arrays. Note that the introduction of saltwater would be a poor idea if one were interested in monitoring salinity or saturation changes, in which case a metallic anti-seize paste or ultrasound gel may also work to increase the electrical contact of the electrodes with the ground around

them. If the soil drains too quickly to add water, these materials might also be helpful, or electrodes can be placed in bentonite or saturated sponges. Below the water table, borehole electrodes are generally in good contact with the formation as a function of the presence of water. In the vadose zone, electrode surface areas may need to be larger to provide good coupling with the subsurface. Contact resistance generally decreases notably as the size of the electrode increases. However, care must be taken not to violate the *point-source approximation* made by most processing codes—where electrodes are assumed to be infinitesimally small points in numerical modeling codes. The actual sizes and shapes of large electrodes may require explicit representation in the numerical model used by the inversion software. A common rule is that the size of the electrode should not exceed 10 percent of the distance between electrodes for the point-source assumption to be approximately valid (e.g., Rücker and Günther, 2011).

3.2   Stacked Measurements

It is common practice for most commercial systems to collect each quadripole several times in a row immediately one after another and average the results. This procedure is referred to as *stacking*. Although collection of stacked measurements nominally increases the duration of the survey, stacking improves the signal-to-noise ratio because noise, if random, is averaged out. In addition, the standard deviation of the stacked measurements (i.e., the stacking error) provides a means to quantify error and define data weights for inversion (although reciprocal measurements described next are preferred). Stacking errors are useful in QA/QC and can be used to weight data in inversion or form a basis for editing datasets prior to inversion. The number of stacked measurements should be recorded on field data collection forms if not recorded by the software. On some instruments, the number of stacked measurements is determined by calculating the running stacking error, with more stacks collected for measurements with larger error.

3.3   Reciprocal Measurements

A *reciprocal* measurement involves swapping current and voltage electrode pairs (Figure 9). In other words, electrodes A and B are used as potential electrodes while electrodes M and N are used as current electrodes; consequently, K_g remains the same. Theoretically, the reciprocal measurement should yield the same resistance (and hence apparent resistivity) no matter the distribution of conductivity in the ground as the regular measurement provided that (1) no sources are present, (2) there are no effects due to contact resistance, and (3) that Ohm's law is linear, with any difference in values indicating instrument error and/or effects in violation of Equation 1 or 5. These measurements should be collected to quantify error in measurements and to check for poorly performing quadripoles, which may then be removed. Apparent resistivities generally should match between stacked or reciprocal datasets within a few percent, if not better. Data

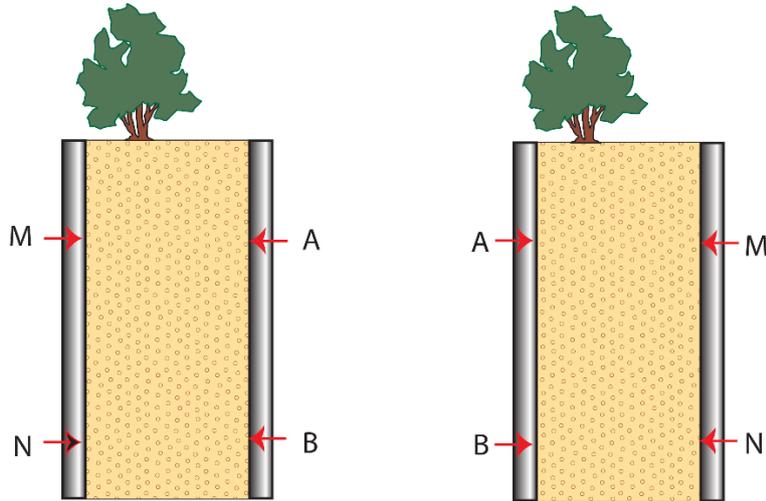corresponding to very low applied currents (e.g., < 10 mA or another cutoff), may also be removed if needed.

Figure 9 - Reciprocal measurements involve swapping the position of the potential and current electrodes, and can be used to identify problems because the reciprocal measurement will yield the same resistivity as the original measurement unless there is a problem or interference.

Different users evaluate reciprocal measurements in different ways, the most common being *reciprocal standard error* and *reciprocity*. If the normal and reciprocal measurements of apparent resistivity are $\rho_{a,1}$ and $\rho_{a,2}$, and the average resistivity is $\rho_{a,ave} = \frac{\rho_{a,1} + \rho_{a,2}}{2}$, the reciprocal standard error s_{recip} and reciprocity r are given by:

$$s_{recip} = \sqrt{\frac{(\rho_{a,1} - \rho_{a,ave})^2 + (\rho_{a,2} - \rho_{a,ave})^2}{2}} \qquad (7)$$

and

$$r = abs\left(\frac{\rho_{a,1} - \rho_{a,2}}{\rho_{a,ave}}\right) \qquad (8)$$

Both the reciprocal error and the reciprocity are useful. Reciprocal errors are used to set data weights in the inversion as explained in Section 0.3. The reciprocity is a dimensionless measure of relative error and, when multiplied by 100, gives the percent error in the reciprocal measurement. It is a useful measure of error for data filtering (e.g., reject all data with a reciprocity larger than 0.10) as is shown in the example in the Data Quality Control and Assurance subsection of Section 5.2.

In general, reciprocal errors are larger than stacking errors, and it is commonly thought that reciprocal errors provide a more comprehensive quantification of noise than stacking errors (Binley et al., 1995). For QA/QC, either reciprocity or reciprocal errors may be used instead of, or in addition to, stacking errors. Depending on the array type, reciprocal measurements may take more time than the regular measurements on multi-channel instruments, which, as mentioned earlier, collect multiple potential

22

The GROUNDWATER PROJECT   ©The Authors   Free download from gw-project.org

Anyone may use and share gw-project.org links. Direct distribution of the book is strictly prohibited.

measurements for each current pair. If *n* potential measurements are made for a single current pair, then *n* reciprocal measurements must be made, each with a different current pair. However, a reciprocal survey for a dipole-dipole array will take exactly the same length of time as the regular survey; this is achieved by running the sequence in the reverse direction of the line. A reciprocal survey for a Wenner array will also take exactly the same length of time as the regular survey as each Wenner measurement requires a separate current injection, so the multi-channel functionality cannot be used for this array. The commonly used Schlumberger array type is an example where reciprocals take much longer, but it is also an example where reciprocity can speed up data collection on a multi-channel instrument (i.e., the inverse Schlumberger array). However, arbitrarily designed sequences often take longer to run as reciprocals when multiple current injections in the reciprocal dataset are needed to reciprocate a set of measurements in the regular survey acquired with a single current injection.

A reciprocal measurement should not be collected immediately after its associated regular measurement, as any residual charge up (polarization) of the current electrodes will affect the voltages recorded between these electrodes with the reciprocal measurement. Such effects generally dissipate in a few seconds, although it may take minutes or longer depending on injection. Reciprocal measurements are best collected either interleaved throughout the measurement sequence file or following regular data collection, depending on whether time-lapse processes are being considered and the subsequent time lag between the regular and reciprocal measurement. For investigations of time-varying processes, collecting a subset of data for reciprocals is preferred because otherwise meaningful temporal changes could appear as error. More information on how to use these data to build an error model can be found in the 2017 paper by Lesparre and others.

The principle of reciprocity also applies to IP datasets. Similar to other aspects of IP data acquisition, acquiring reciprocal IP datasets is more challenging than acquiring reciprocal ER datasets. The polarization of a recently used current electrode may severely corrupt the reciprocal IP measurement. IP errors can instead be quantified through analysis of the shape of the decay curves following current shut off (Flores Orozco et al., 2018). However, reciprocation of IP datasets can be done with careful attention to data acquisition to ensure dissipation of IP effects, resulting in significantly improved confidence in IP datasets, which are traditionally susceptible to errors and misinterpretation (Slater and Binley, 2006; Zarif et al., 2017).

3.4   Error Considerations for Time-Lapse Measurements

In the case of time-lapse imaging, collecting multiple background datasets can be useful for determining systematic errors and is generally well worth the time, as the most time-consuming part of ER data collection usually is deploying the electrodes and cables, and understanding the background conditions is important to interpreting changes. In systems where a hydrogeologic change is being introduced (infiltration or a tracer test, for

instance), collecting multiple background datasets provides some measure of natural variability before the introduction of that change. In cases where fast time-lapse data are needed, collecting a subset of reciprocals—or collecting *repeat measurements* to get errors between two complete data sequences, one collected right after the other—may be a valuable way to get another measure of error beyond stacks. An example of time-lapse monitoring is provided in Section 0.2.

3.5   Pulse Duration

Some time-domain instruments allow the user to select the duration of the current injection. Commonly, *pulse duration* varies from 250 milliseconds (ms) to several seconds. Lower pulse duration results in shorter data acquisition time, but longer pulse duration may be key to achieving steady state voltages and thus data more consistent with the physics assumed for analysis (e.g., the Poisson Equation). Similar issues arise in hydrogeology when performing hydraulic analysis based on steady-state assumptions (e.g., Thiem-Equation based analysis), where pumping continues until a quasi-steady state is achieved and then measurements are made. Otherwise, transient analysis is necessary, for example, Theis-Equation-based analysis in the groundwater analogy and IP in electrical imaging. Pulses on the order of 250 ms may be acceptable when exclusively collecting ER data in conductive, low-clay media. In the presence of clays and other chargeable media, however, longer durations may be required to achieve equilibrium voltages. Acquisition of IP datasets generally requires longer pulse durations (1 s or greater is recommended) so that the sufficient discharge (or charge up) occurs to be reliably recorded. As an approximate guide, the acquisition of high-quality IP data is likely to increase the survey time two to three-fold over acquisition of only ER data. The length of the pulse duration can be varied, and surveys repeated, to determine the minimum duration necessary to achieve good data.

3.6   Notes on Field Conditions

Notes on the location of electrical lines, radio transmission towers, known metallic objects, topography, and weather should be collected at each field site, as should decisions about the QA/QC procedures above. It is important to check and record: battery voltages, *x-y-z* positions of the electrodes, how their position was determined (meter tape, GPS, laser level, etc.), and how the electrodes were deployed and/or built. The integrity of multi-core cables should be assessed, particularly around individual electrode takeouts that are most prone to damage during use. For cross-well measurements, information on well construction (casing length, total depth, borehole integrity, presence of monitoring equipment, etc.) should be known prior to installing cables and injecting current. Some commercially available systems provide a test resistor to verify the correct operation of the instrument. Results of this test, if performed, should be recorded. Although outside the scope of this book, safety is an important consideration when dealing with any electrical

24

instrumentation, and equipment users should develop protocols to ensure that no one touches energized electrodes during data collection. These issues do not prevent collection of quality data, but should be recorded and considered when evaluating data quality.

4   Data Inversion

4.1   The Goal of Inversion

Once electrical imaging data are collected, they are inverted to obtain a spatially discretized (i.e., gridded or meshed) distribution of the electrical properties of the subsurface. In the case of ER measurements alone, it is just the electrical conductivity structure that is estimated by the inversion. When IP datasets are acquired, both the electrical conductivity and the intrinsic chargeability (or the intrinsic phase) structure are estimated, and IP data cannot be inverted without ER data. With IP datasets, images can be presented in terms of the real and imaginary components of the complex conductivity. Irrespective of what data have been acquired—whether ER data alone, or ER and IP data combined—the inversion of electrical imaging datasets involves a number of common key steps/concepts. For simplicity, we describe the inversion process from the perspective of an ER dataset alone, but the mechanics and considerations introduced in this section apply equally to combined ER and IP datasets.

The goal of inversion of an ER dataset is to recover a subsurface distribution of electrical conductivity (Figure 10), $\sigma_{x,y,z}$ (note for frequency domain, IP this would be $\sigma^*_{x,y,z}$) that could have produced the observed data (step 2 and 3 below). The general procedure for inverse modeling consists of the following steps:

1. Start with a distribution of electrical conductivity (typically a homogeneous starting model corresponding to the average apparent conductivity measured in the field);

2. Use a forward simulator which, for the given distribution of electrical conductivity, calculates predicted data using Equation 1 (or Equation 5 for frequency-domain IP, and time-domain IP with caveats as noted below);

3. Calculate the misfit between the predicted and the observed data and also a measure of the complexity (e.g., roughness) of the electrical conductivity distribution; and

4. If the misfit is less than our stopping criteria, stop and accept the current subsurface distribution of electrical conductivity as the final result. If not, modify the model to improve the fit, and return to step 2.
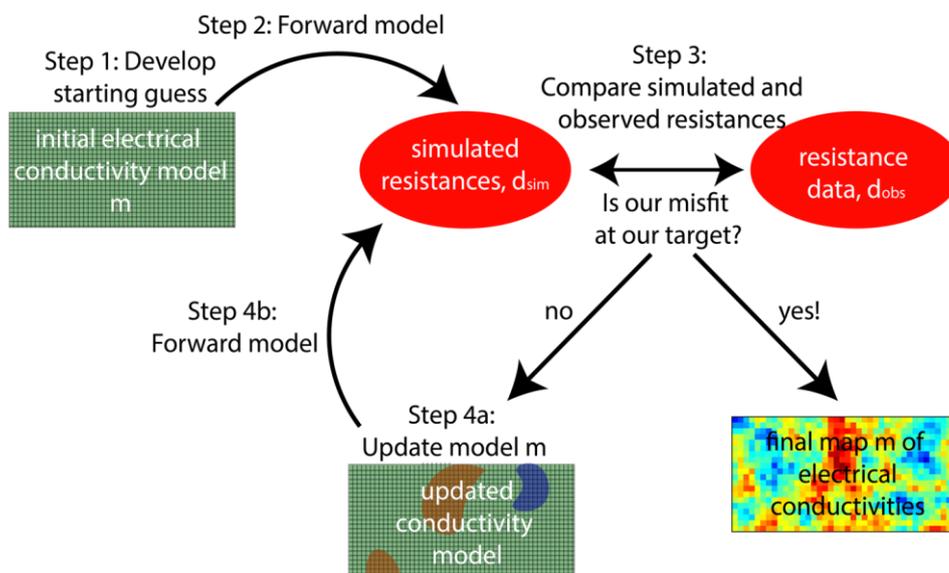
Figure 10 - A simplified overview of the inversion process.

In inversion codes, forward models are called repeatedly within an optimization framework to calculate predicted data for comparison with observed data. The optimization iteratively updates the model to improve the match between predictions and observations. Data processing and inversion can be performed with commercially available software packages such as AGI EarthImager (LaBrecque and Yang, 2001), Res2DInv (Loke and Barker, 1996), or MPT ERTLab, and public-domain or freeware packages such as RESINVM3D (Pidlisecky et al., 2007), E4D (Johnson et al., 2010), ResIPy (Blanchy et al., 2020), pyGIMLIi (Rucker et al., 2017), or SimPEG (Cockett et al., 2015). The majority of these codes also permit the inversion of IP datasets. It is not our goal to review or compare these codes, but most follow similar inversion approaches, which are based on Gauss-Newton, quasi-Newton or steepest-descent algorithms (Tarantola, 1987), with some codes supporting use of multiple inversion algorithms. Depending on selection of modeling and inversion parameters, these codes generally can be made to produce similar results. Default values differ greatly, however, and it is not always clear how parameters are used within the inversion. Selection of many inversion settings can be somewhat subjective and should be guided by prior knowledge of the site geology or the nature of the targets. For example, in a layered system, one might choose to apply anisotropic smoothing, which will result in a tomogram that has a layered character. For results to be reproducible, it is critical to (1) report all parameter selections including default values, (2) document the algorithm used by the software, and (3) archive a copy of the software code or executable. Justifications of parameter choices should also be documented. An example of how inversion settings affect tomograms is demonstrated in Section 0.2. The process for selecting inversion settings should be guided by prior information, and many hydrogeologists will find it useful to work with a geophysicist while learning inverse techniques for these data.

Ideally, the inversion should result in the true distribution of electrical conductivities of the subsurface. In practice, this is impossible for several reasons. First, the electrical conductivity estimates are commonly produced for blocks with dimensions of tens of centimeters to several meters on the side, while earth conductivity varies on much smaller scales. Thus, the best one can hope for is to identify block conductivities that represent some sort of weighted, spatial averages. Additionally, there commonly is not enough information in the data to uniquely determine all the block bulk conductivity parameter values. Unlike medical imaging, where it is possible to acquire a 360-degree view around the target, ER is usually limited to surface and borehole electrodes unless working on soil cores or experimental tanks, which is partly why medical imaging offers higher resolution compared to geophysical imaging. The result of this limited available information is called *ill-conditioning*, which is a property of matrix-inversion problems where limited data sensitivity to parameter values causes uncertainties in the data (e.g., resistance measurements) and can lead to large errors in the parameter estimates (e.g., electrical conductivity values). This ill conditioning is typically rectified through model *regularization*, which imposes additional constraints on the estimated model to get a unique set of stable solutions, as described subsequently. Additionally, as noted above, depending on the discretization of the finite-difference grid or finite-element mesh used for numerical approximations of Equation 1 or 5, some quadripoles may model poorly. For example, the inverse model would not be able to accurately match these data. Finally, accurate representation of data errors (for example using reciprocal measurements or stacking described above) is needed to ensure quality inversion results that do not over- or under-fit measurements.

Resistivity software packages that incorporate time-domain IP measurements model the distribution of the intrinsic chargeability in addition to electrical conductivity. In contrast, frequency-domain measurements are processed with algorithms that model the complex electrical conductivity distribution per Equation 5. The electrical conductivity magnitude and phase, or the real and imaginary parts of the complex electrical conductivity, can be imaged. The measured apparent chargeability and measured apparent phase are directly proportional to each other, although the proportionality constant will vary depending on how a time-domain instrument is configured (Slater and Lesmes, 2002). Consequently, time-domain measurements can be modeled using Equation 5 if this proportionality constant is defined (Mwakanyamale et al., 2012).

4.2 Regularization in Electrical Imaging Inversion

Most tomographic problems in geophysics are solved with an excess number of model parameters and use regularization to create a mathematically stable solution (e.g., Constable et al., 1987). Due to these issues, this non-linear problem is solved using iterative inversion (Tripp et al., 1984; Daily and Owen, 1991). The solution to the ER inverse problem is a cross section or volume of electrical conductivity values and is usually based on

non-linear least-squares minimization of a two-part objective function, *F*, which is given by Equation 9a.

$$F = \left\| C_D^{-0.5}(d_{obs} - g(m)) \right\|^2 + \varepsilon \|Dm\|^2 \tag{9a}$$

This can also be written as Equation 9b.

$$F = \left(d_{obs} - g(m)\right)^T C_D^{-1}(d_{obs} - g(m)) + \varepsilon m^T D^T D m \tag{9b}$$

where (for the case of ER inversion alone):

d_{obs} = vector of electrical resistance ($\Delta V/I$) or apparent resistivity measurements, where the vector length is equal to the total number of quadripoles.

$g(\ )$ = forward model for electric potential (Equation 1 or 5), which produces the simulated estimates of the measurements.

m = vector of parameter estimates, (log electrical conductivity).

C_D = covariance matrix of data uncertainty or errors (often where the diagonal of the matrix is defined by reciprocal or stacked measurements, and the off-diagonal values are zero), which defines how certain we are in our measurements. This matrix often includes some measure of modeling errors, as described in Section 4.3 below.

ε = regularization parameter that determines the importance given to the smooth appearance of the electrical conductivity field relative to the misfit between calculated and observed resistances. An overly small ε will minimize the residual error between measured and modeled resistances and may overfit the data, producing spurious heterogeneity in the solution. In contrast, an overly large ε will identify an overly smooth electrical conductivity field that may not fit the measured field data (resistances) well (see, for example, Tikhonov and Arsenin, 1977).

D = model-weighting regularization matrix, which can either be defined by a discretized spatial-derivative operator or be based on the covariance of the model parameters (Tarantola, 1987; Gouveia and Scales, 1997; Kitanidis, 1997; Vasco et al., 1997; Day-Lewis et al., 2003). This matrix defines how each pixel is related to one another.

The first part of the objective function is the *data misfit* term, which minimizes the discrepancy between field resistance data (or resistance and IP data for IP inversion) and the computed resistances (or resistances and IP measurements for IP inversion) based on Equation 1 or Equation 5, within measurement errors. The second part is the regularization term, often called the *model roughness* if smoothing is sought, which typically minimizes the roughness (or maximizes the smoothing) of the electrical conductivity field and allows for a well-posed inverse problem. This term is required due to the *overparameterization* of the

29

inverse problem, meaning that the information provided by the measurements cannot uniquely resolve each of the conductivity parameters. It is possible to be creative with the regularization term, depending on prior information available to develop a conceptual model (e.g., Caterina et al., 2014; Nguyen et al., 2016; Hermans et al., 2016).

In a non-linear inverse problem, model parameters are updated iteratively by repeated solution of a linearized system of equations for Δm at successive iterations. Such an approach results in the regularization changing throughout the iterative process. This process makes it difficult to map the effect of regularization throughout the inversion process, and consequently impairs quantitative inference from the images. The update appears as shown in Equation 10.

$$[J^T C_D^{-1} J + \varepsilon D^T D]\Delta m = J^T C_D^{-1}(d_{obs} - g(m_{k-1})) - \varepsilon D^T D m_{k-1} \tag{10a}$$

$$m_k = m_{k-1} + \Delta m \tag{10b}$$

where:

J = Jacobian matrix at iteration k, with elements $J_{ij} = \dfrac{\partial d_{sim,i}}{\partial m_j}$

m_k = vector of parameter estimates after updating in iteration k

Δm = vector of parameter updates for iteration k

Although tomographic inversion with regularization is useful for imaging large-scale (low-spatial-frequency) structures, it yields poor results when attempting to infer quantitative values from the recovered images (e.g., Binley et al., 2002; Singha and Gorelick, 2005; Day-Lewis et al., 2007) due to uncertainty in the inversions for reasons discussed in the next section.

3-D acquisition and inversion are increasingly possible and appropriate, although many practitioners still use 2-D inversion. As noted earlier, commercially available software for 2-D inversion commonly invokes the 2.5-D assumption for computational efficiency, where 2-D ER cross sections are constructed by simulating 3-D current flow under the assumption of 2-D heterogeneity (Dey and Morrison, 1979; LaBrecque et al., 1996). The 2.5-D assumption amounts to assuming that all heterogeneity in the 2-D imaged cross section extends infinitely out the 2-D plane. Clearly, this assumption is violated in the presence of strong 3-D heterogeneity, which requires 3-D acquisition and inversion approaches to image accurately.

4.3   Selection of Inversion Parameters to Prevent Overfitting/Underfitting of Data

Data should generally be weighted based on their measurement (reciprocal or stacking) uncertainty (Sections 3.2 and 3.3) to prevent overfitting or underfitting of the data. In other words, the inversions should generally match the data within the uncertainties

(sometimes called errors) quantified by reciprocal or stacking errors. However, there are often systematic data or model sources of error that are not manifested in reciprocal or stacking errors. For example, systematic sources of data error can arise from electrode position errors or temporal variation in subsurface electrical conductivity over the course of the survey. Systematic model errors include coarse-grid error (i.e., the inability of the model to simulate the effects of sub-grid heterogeneity), or violation of the 2-D heterogeneity assumption in 2-D inversions as noted above. We usually cannot quantify these errors and therefore cannot account for them via data weighting; their existence can produce inversion artifacts if they are not accounted for. The sources and magnitudes of these errors are often unknown and therefore require a subjective estimation of how to approach error weighting by the user.

One common approach to estimating data error is given by Equation 11.

$$s_i = a_i\big(\text{abs}(R_i)\big) + b \tag{11}$$

where:

s_i = standard deviation of resistance measurement i

a_i = unitless scaling factor giving the error in terms of the magnitude of the measured resistance R_i

b = small resistance indicating the precision of the voltmeter

As written, Equation 11 allows for a different value a_i for each resistance measurement i, where the a values initially could be based on the reciprocal or stacking error expressed as a decimal fraction. These values can be increased until the inversion converges to a reasonable conductivity structure, at which point additional sources of error would presumably be accounted for. This approach assumes that standard or reciprocal errors are proportional to total error. Alternatively, a single a is often used to establish representative weights for all resistance measurements in cases where individual error weights are too low. In this case, it is common to first calculate average reciprocal errors for a range of bins that divide up the reciprocals in terms of increasing resistance (Figure 11). The reciprocal error for any resistance value is then determined from the equation of the line. One way to test whether reciprocal and stacking errors adequately represent the true data error is to first invert the data under the hypothesis that reciprocal/stacking error adequately quantifies all sources of error. If the inversion (1) does not converge (i.e., cannot fit the data) in a reasonable number of iterations, (2) results in an overly heterogeneous electrical conductivity structure, or (3) produces unrealistic electrical conductivity values, then it is likely that the reciprocal and stacking errors do not adequately capture the true error. In this case, the user must increase the error to produce smoother or more uniform tomograms. Use of the correct errors will result in convergence within a reasonable number

of iterations, typically 3 to 10, although this will depend strongly on the inversion algorithm.
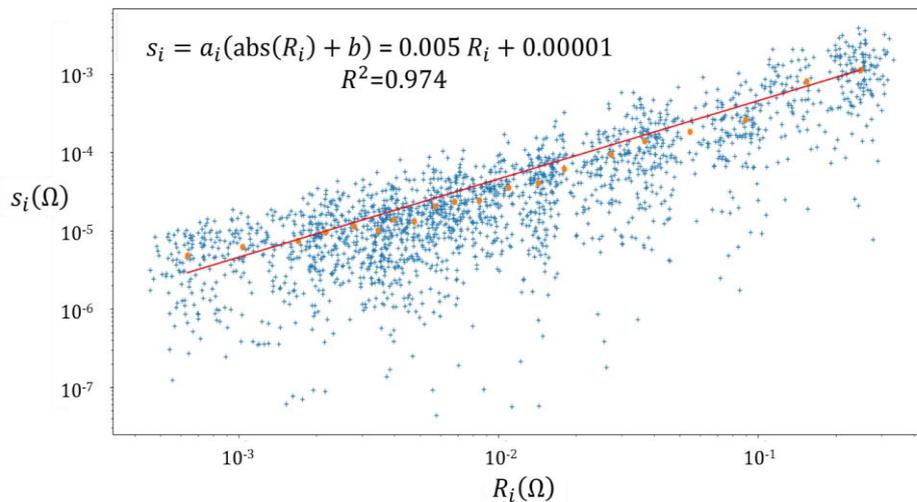

Figure 11 - Example reciprocal error plot for an electrical resistivity dataset. Blue crosses are individual reciprocal errors whereas orange dots are average values for bins defined in terms of increasing resistance. The linear fit of an estimated reciprocal error (s_i) as a function of resistance R_i is based on the binned values. Plot created with ResIPy (Blanchy et al., 2020).

There are several approaches commonly used to set the relative weighting between the model roughness and data misfit in the inversion (Equation 9a and b), i.e., the value of ε. This issue is not trivial, as the tradeoff between terms of the objective-function controls the variability of estimated electrical conductivity and, ultimately, whether the information in the data is optimally utilized. If too much weight is ascribed to the model roughness term, underfitting occurs—thus the inversion does not capitalize on all the information provided by the data, resulting in an overly smooth tomogram. On the other hand, if too much weight is given to the data misfit term, overfitting results—the data are fit so well that the inversion reproduces noise, resulting in an overly complex tomogram with spurious structure and possibly unrealistic electrical conductivity values. While these models are mathematically viable and may even fit data better than other models, they are geologically unrealistic and this is where the art of inversion and prior knowledge of the system are important.

The *tradeoff parameter*, ε, is analogous to a contrast knob, which if set incorrectly results in an image that is washed out at one extreme or noisy at the other. The simplest approach to identify ε is subjective selection by the user, such that the resulting tomogram is qualitatively consistent with existing knowledge of the range of subsurface electrical conductivity and geologic structure. More objective approaches include an Occam's inversion (Constable et al., 1987), the L-curve (Hansen and O'Leary, 1993), and generalized cross-validation (GCV) (e.g., Haber and Oldenburg, 2000; Farquharson and Oldenburg, 2004). In general, the three techniques produce similar results for most datasets. These three approaches are:

32

The GROUNDWATER PROJECT   ©The Authors   Free download from gw-project.org

Anyone may use and share gw-project.org links. Direct distribution of the book is strictly prohibited.

- In Occam's inversion, ε is determined as part of the optimization to achieve the smoothest model that matches the data to the desired misfit.
- In the L-curve approach, the inversion is repeated for a number of values of ε, and a plot of model complexity versus data misfit (i.e., the second term of Equation 9a and b versus the first term of Equation 9a and b) is constructed. The optimal ε is taken as the value at the elbow of the resulting L-shaped curve.
- In GCV, the tradeoff parameter is identified based on a procedure analogous to inverting the dataset repeatedly, leaving one measurement out at a time, and finding the value for ε that minimizes the average prediction error for the data eliminated.

An inversion converges when the data misfit is reduced to some set value. Criteria for computing the data misfit commonly are based on the *absolute weighted error* (*AWE*), sometimes called the *normalized error* or the *percent error* (*PE*), which for measurement *i* are given respectively as Equations 12a and 12b.

$$AWE_i = \frac{((d\_(obs,i) - d\_(sim,i)))}{\sqrt{(C\_(d,i))}} \tag{12a}$$

$$PE_i = \frac{100\%\left(d_{obs,i} - d_{sim,i}\right)}{d_{obs,i}} \tag{12b}$$

where:

$d_{obs,i}$ and $d_{sim,i}$ = observed and simulated values of datum *i*

$C_{d,i}$ = variance of datum *i* as determined by the data noise estimate

AWE and PE = used to compute the normalized chi-squared (χ^2) value and the root-mean-squared error (*RMS*) value defined by Equation 13a and 13b respectively.

$$\chi^2 = \frac{1}{N}\sum_{i=1}^{N} AWE_i^2 \tag{13a}$$

$$RMS = \sqrt{\frac{1}{N}\sum_{i=1}^{N} PE_i^2} \tag{13b}$$

where:

N = number of data

The normalized χ^2 value is a linear scaling of the first term of the objective function (Equation 9a and b). It is a useful measure of data misfit because it gives a direct indication of what the inversion is trying to minimize (in addition to the regularization term) and includes the covariance of the data (the error weights) directly. When the data misfit in the numerator of the AWE is consistent with the data error estimate in the denominator of the

AWE, then $\chi^2 = 1$. Assuming our data are appropriately weighted, then $\chi^2 = 1$ is the target value we are aiming for at convergence. That is, we would ideally fit our observed data with our simulated data in a manner consistent with the uncertainty in the measurements. The RMS (root-mean-squared error) value (as defined in Equation 13b) is equivalent to the standard deviation of the PE distribution, and therefore provides an intuitive measure of the total data misfit in terms of percent error, with no covariance term. Also, in contrast to the χ^2 value, the RMS value is independent of data weighting. Consequently, it is possible to have a χ^2 close to 1 but a very large RMS error if the covariances are large.

Some software packages assume the inversion has converged when the data misfits are within the limits specified by the data error, as outlined above. Other packages support Occam's inversion or use of the L-curve approach. Yet other packages leave it to the user to decide when the inversion has converged, placing the burden of balancing the tradeoff between the model and data misfit on the scientist's subjective judgment. In any case, all selections of inversion parameters should be recorded and reported. Some examples of under- and overfitting are provided in the case studies in Section 0.

4.4   Definition of Data Misfit

In Equation 9a and b, the data misfit is based on an *L2 norm* (i.e., as the sum of weighted, squared differences between predicted and observed values), which is the first term in the equations. The L2 norm is highly sensitive to outlier data, hence the need to carefully edit datasets and remove data corresponding to electrodes with poor electrical contact or faulty channels. Many inversion packages also support minimization of the L1 data misfit, which has been referred to as *robust inversion*. The L1 norm is based on absolute differences instead of squared differences and is therefore less sensitive to outliers (Claerbout and Muir, 1973). The L1 norm can also be applied to the regularization term of Equation 9a and b instead of the L2 norm, which tends to produce blocky inversion results with sharp boundaries. Implementation of the L1 norm on either the data misfit or regularization term of the objective function require re-weighting of C_D and/or D respectively at each outer iteration of an iterative least-squares solution. This is commonly referred to as Iteratively Reweighted Least Squares inversion (Farquharson and Oldenburg, 1998).

4.5   Quantification of Inversion Quality

Several approaches are commonly used to gain insight into the reliability of tomograms. For small inverse problems, it is possible to calculate the model resolution matrix (e.g., Menke, 1984) and present the diagonals, rows, and columns of these matrices as cross-sectional images. Conceptually, the *model resolution matrix* is the lens or filter through which the inversion *sees* the study region. For a linear inverse problem, the parameter estimates are expressed by Equation 14.

$$m = [J^T C_D^{-1} J + \varepsilon D^T D]^{-1} J^T C_D^{-1} d_{obs} \approx [J^T C_D^{-1} J + \varepsilon D^T D]^{-1} J^T C_D^{-1} J m_{true} \qquad (14)$$

In this case, the model resolution matrix R is defined as shown in Equation 15.

$$R = [J^T C_D^{-1} J + \varepsilon D^T D]^{-1} J^T C_D^{-1} J \qquad (15)$$

Consequently, the parameter estimates are the product of the true parameter values and the resolution matrix as shown in Equation 16.

$$m = R m_{true} \qquad (16)$$

For linear problems, where J is independent of m_{true}, R can be calculated prior to data collection. Given an estimate of measurement errors, the model resolution matrix can be calculated using Equation 15 and used as a tool to assess and refine hypothetical survey designs and regularization criteria. In interpreting inversion results, R is useful for identifying likely inversion artifacts (Day-Lewis et al., 2005). The model resolution matrix quantifies the spatial averaging inherent to tomography; hence, it gives insight into which regions of a tomogram are well resolved versus poorly resolved. This information is valuable if tomograms are to be converted to quantitative estimates of porosity, concentration, or other hydrogeologic parameters. Calculation of resolution matrices, however, remains computationally prohibitive for many problems, particularly those involving 3-D inversion. Hence, few commercially available software packages support calculation of R, and it is instead more common to look at an inverse problem's cumulative squared sensitivity vector (S) as shown in Equation 17.

$$S = diag(J^T J) \qquad (17)$$

Here, J is the sensitivity matrix defined in Equation 10a and $diag()$ indicates the diagonal elements of a matrix. The sensitivity matrix can be used to gain semi-quantitative insight into how resolution varies spatially over a tomogram. Pixels with high values of sensitivity are relatively well informed by the measured data, whereas pixels with low values of sensitivity are poorly informed. It is important to note that, in contrast to R, S does not account for the effects of regularization criteria (as contained in D) or measurement error (as contained in C_D). Rather, S is based only on the survey geometry and measurement sensitivity. An example sensitivity map is provided in the case study in Section 5.2 and qualitatively in Figure 4. Another question is whether inversion results are consistent with our conceptual models of the site—this is a different definition of inversion quality. A good review exploring this idea is presented by Linde (2014).

4.6   Checks on Inversion Results

Tomographic inversion results are strongly affected by selected inversion parameters and regularization criteria, especially in the presence of large measurement errors. It is instructive, therefore, to run multiple inversions to gain insight into the effects

of different software settings, which is the philosophy of the depth of investigation (DOI) analysis seen earlier. Rarely are default inversion settings appropriate and the inversion should be guided by prior information. Prior information that may be useful includes past geophysical results, (hydro)geologic maps, and drillers' logs. If inverted electrical conductivity cross sections are inconsistent with such prior information, this could indicate that settings are suboptimal or that assumptions (e.g., 2-D heterogeneity) are violated. **Table 1** lists some common problems and their associated symptoms and solutions. We emphasize that **Table 1** is by no means exhaustive in terms of the symptoms, problems, and solutions and relationships between them. Rather, this is meant as a starting point for practitioners to begin thinking about the roles of various inverse settings.

Table 1 - Common problems with inversion settings, and the associated symptoms and solutions.

Symptom	Possible problems	Solution
Minimum/maximum estimated electrical conductivity too low/high compared to expected values	The inversion may be overfitting the data	• Stop inversion at an earlier iteration or increase the assumed measurement error
	Non-random outlier data may be present	• Check the dataset for outliers and edit • Try the L1 norm for data misfit
Tomogram is speckly or looks like a checkerboard	The inversion may be overfitting the data	• Stop inversion at an earlier iteration or increase the assumed measurement error in an Occam's inversion
	Non-random outlier data may be present	• Check the dataset for outliers and edit • Try the L1 norm for data misfit
The inversion cannot match the data to within the reciprocal error	The optimization algorithm may be caught in a local minimum	• Change optimization tolerances • Increase number of iterations • Update the Jacobian more frequently • Change the starting model
	The finite-difference or finite-element grid may be too coarse	• Refine the grid or mesh
	The inversion grid may be too coarse	• Increase the number of inversion parameters
	Non-random outlier data may be present	• Check the dataset for outliers and edit • Try the L1 norm for data misfit
The tomogram does not look like expected geology	Regularization criteria may be smoothing/blunting the tomogram too much	• Try robust model misfit instead of L2 model misfit • Use anisotropic regularization • Try different regularization criteria
	Electrical conductivity may not correlate with lithology	• Another geophysical technique may be needed

36

Symptom	Possible problems	Solution
	Resolution may be above the scale of the pertinent heterogeneity.	• Another geophysical technique may be needed or array type and/or electrode spacing used may need to be reconsidered
Two (or more) tomograms that share a borehole appear inconsistent at the borehole	Electrical anisotropy	• Use an inversion package with a forward model that allows for electrical conductivity anisotropy
	Outlier data are present in at least one dataset	• Check the dataset for outliers and edit • Try the L1 norm for data misfit
	Parsing data into individual tomograms when they should be considered together	• Invert all data at once, rather than breaking it into pieces
Tomograms show vertical streaking, or high or low electrical conductivity patches only at boreholes	Resolution may vary greatly from the sides to the middle of the tomogram	• Create synthetic or hypothetical forward models of the experiment to evaluate resolution and likely artifacts • Examine plots of the inversion's sensitivity or resolution matrix • Explicitly model the boreholes

5 Case Studies

5.1 2-D Waterborne Resistivity and Induced Polarization Profiling

Background

Here, we outline the case study of 2-D electrical resistivity and induced polarization imaging reported in the 2010 paper by Slater and others, which focused on improving understanding of the hydrogeological framework regulating exchange of groundwater with surface water of the Columbia River at the United States Department of Energy Hanford 300 Facility, Richland, Washington, USA. The basic hydrogeological setting consists of a coarse-grained aquifer (the Hanford Formation) underlain by a lower permeability, fine-grained confining unit (the Ringold Formation). A legacy of nuclear waste processing and disposal at the site extending through the Cold War era resulted in significant potential for radionuclide-contaminated groundwater to discharge into the Columbia River. The existence of relict paleochannels incised into the Ringold Formation had previously been proposed to provide preferential flow paths promoting rapid transport of contaminants from the aquifer into the river. The risks of radionuclide contamination led to a high cost of drilling at this site, encouraging the use of geophysical surveys to understand the structure of the region of interaction between surface water and groundwater. Waterborne surveys have been successfully used to investigate coastal processes and groundwater-surface water exchange in other systems (e.g., Day-Lewis et al., 2006).

Data Collection

Two-dimensional resistivity and induced polarization imaging surveys were performed to improve estimates of the spatial variability in the depth to the contact between the Pleistocene Hanford formation and the Pleistocene Ringold Formation. The surveys were designed to explore for evidence of incisions into the Ringold Formation that might represent the location of high-permeability paleochannels. The rationale for the application of IP was a suspected strong contrast in polarizability between the coarse-grained, Hanford sediments (low polarizability) and the fine-grained Ringold sediments (high polarizability). The acquisition of ER measurements alone would have been less informative because of the expected influence of variations in the groundwater electrical conductivity due to variable surface water-groundwater interaction on the electrical images.

To rapidly image a long reach of the river corridor, measurements were acquired using a floating array of 13 graphite electrodes spaced at 5 m intervals pulled behind a boat. In this study, ER and IP measurements were performed on approximately 30 km of 2-D line profiles in water depths varying from 2 m to 18 m. Data were collected in July 2008 from a Gregor aluminum-hull jet boat, using a 10-channel time-domain ER/IP instrument (Syscal

Pro, Iris Instruments, France) as shown in Figure 12. This time-domain instrument records the apparent integral chargeability (Equation 4) determined from the decay curve after current shutoff. Measurements were recorded every 0.5 to 3.0 m depending on survey speed, resulting in more than 65,000 measurements over the 30 km of line.
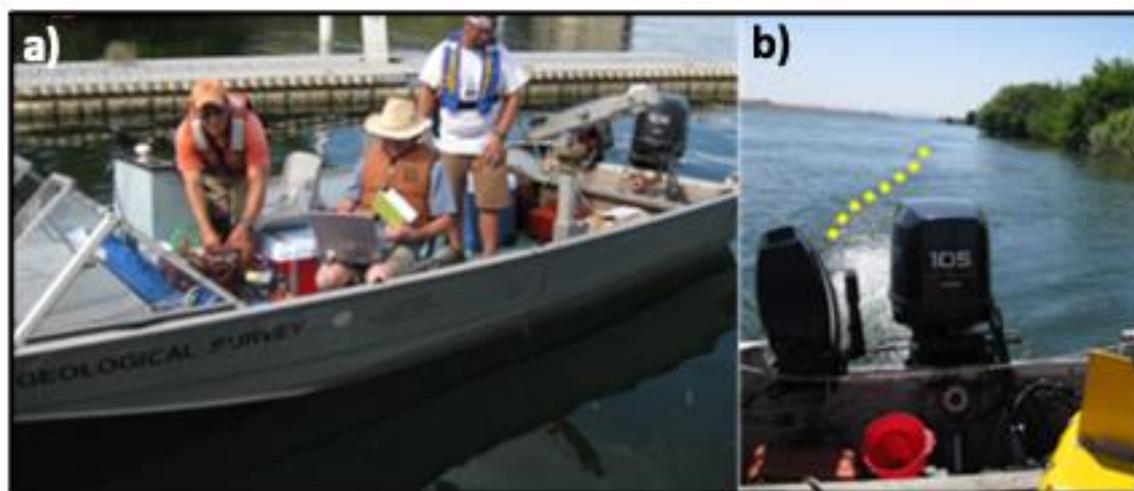

Figure 12 - Photographs of deployment of waterborne resistivity and induced polarization data acquisition at the Hanford site. a) Gregor jetboat used for data acquisition, b) deployed floating array concept (yellow symbols depict 8 of 13 electrodes, remaining 5 are closer to boat).

Data Processing

The waterborne resistivity measurements were inverted for an estimated subsurface distribution of electrical conductivity and chargeability using the commercially available RES2DINV package (Loke et al., 2003). The variable-thickness water layer was constrained to a uniform conductivity and zero chargeability (water is non-polarizable at low frequencies). The dataset was treated as a series of near-parallel 2D lines for individual inversions. Electrode locations were calculated from a GPS located on the boat and knowing the length of the electrode takeouts on the cable pulled behind the boat. Each line was then inverted using the conventional smooth regularization constraint except for the fixed/known surface water layer.

Data Interpretation

Figure 13 shows the 2-D inversion of one line (Line 20 approximately 20 m from the shore). The inverted electrical resistivity distribution (lower panel) and the inverted normalized chargeability ($Mn = M/\rho$) (upper panel) are shown. This normalization of the chargeability by the resistivity provides a direct measure of the polarizability that is unaffected by variations in pore fluid conductivity of the groundwater and therefore is exclusively related to the physical properties of the sediments (Slater and Lesmes, 2002). The riverbed is shown as a black line.
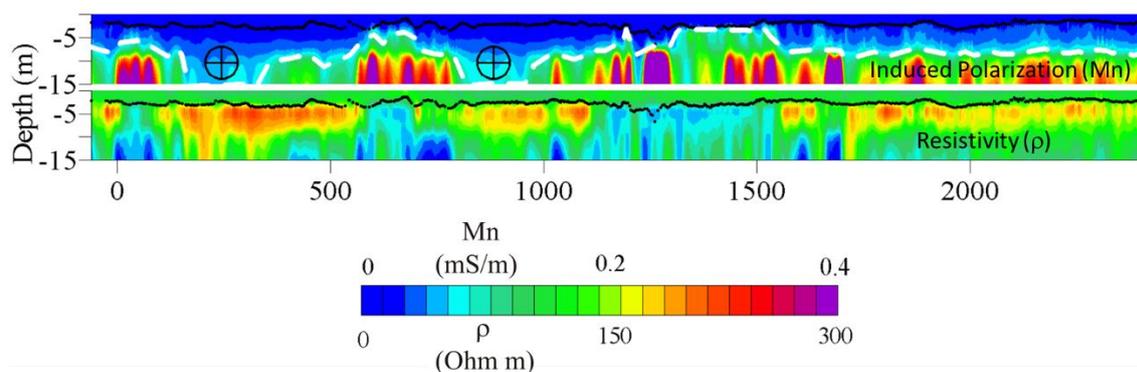
Figure 13 - 2D resistivity and induced polarization image acquired along a 3 km section of the Columbia River, WA, USA corridor. Black solid line is base of water layer and white dashed line is interpreted contact between aquifer and underlying confining unit. Crosshairs denote suspected paleochannels incised below the contact of the aquifer with the confining unit. Modified from Slater and others (2010).

Beneath the riverbed, the resistivity image is primarily composed of a higher resistivity layer underlain by a low resistivity layer that appears to come into contact with the riverbed between 1100-1500 m along the line. The upper resistive layer was interpreted as the coarse-grained, Hanford formation sediments with the lower, more conductive layer representing the finer-grained Ringold Formation sediments. The IP image (normalized chargeability) provides a much clearer picture of this hydrogeological structure. The water layer and the coarse Hanford formation sediments are both low polarizability whereas the fine-grained Ringold sediments are highly polarizable. From this IP image, the variation in the depth to the Hanford-Ringold interface along this portion of the river corridor is highlighted (white dashed line). The IP image reveals strong evidence for the location of at least two coarse-grained paleochannels incised into the Ringold sediments (black crosshairs). One of these paleochannels was subsequently mapped with ER and IP measurements performed inland (Mwakanyamale et al., 2012). Overall, this 2-D ER and IP survey notably improved understanding of the hydrogeological framework along this important river corridor.

5.2   4D Resistivity of a Biostimulation Experiment

Time-lapse inversion is frequently used to map changes in electrical conductivity through time, as might be expected from processes such as infiltration of water into dry soils or tracer transport (Figure 14). Here, we demonstrate the steps taken for data collection in the field and the impacts of inversion decisions using a case study at the former Brandywine Defense Reutilization and Marketing Office (DRMO), which is an inactive 3-hectare facility administratively controlled by Andrews Air Force Base (AAFB) and located approximately 13 kilometers south-southeast of AAFB in Brandywine, Maryland, USA. The Brandywine DRMO yard was used from 1943 to 1987 for temporary storage of scrap materials and hazardous waste generated from various Department of Defense facilities in the region and is currently classified as a Superfund site. The primary groundwater contaminant at the former DRMO is trichloroethylene, which has spread beyond the AAFB

40

property into adjacent commercial and residential properties (United States Air Force, 2006). We note that this case study shows the state of the art in terms of data collection, inversion, and analysis, especially for a 4-D system, rather than the state of the practice, which remains 2-D static inversions at the time of this writing.
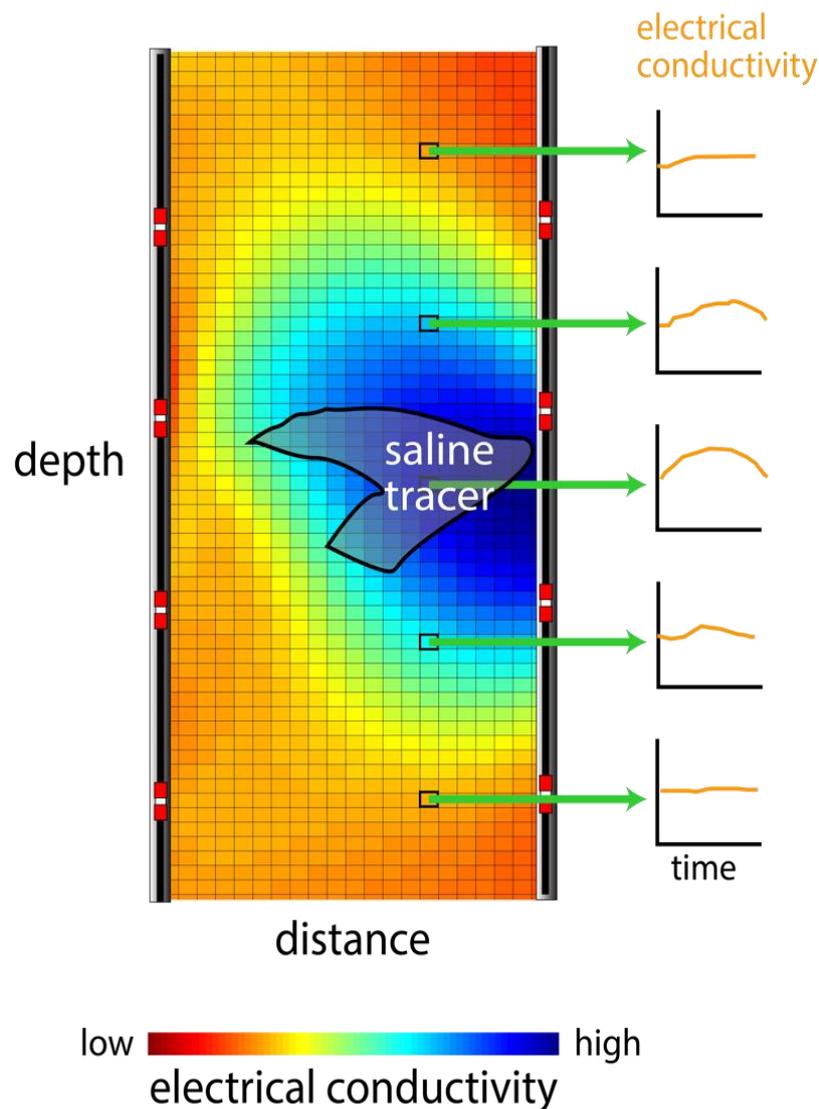

Figure 14 - Schematic of a cross-well inversion from a system with active changes—in this case, the movement of an electrically conductive tracer. By looking at a series of inversions through time, we would see changes in conductivity at particular pixels, as demonstrated by the "pixel breakthrough curves" (e.g., Slater et al., 2000) on the right.

To remediate groundwater contaminants at the site, a biostimulation effort commenced in 2008. This effort involved injecting amendments into the subsurface to enhance microbial activity associated with contaminant biodegradation. An autonomous cross-well ER monitoring system was installed at the site to demonstrate and validate the utility of geophysical measurements for providing timely and actionable information on the spatiotemporal behavior of amendments injected into the subsurface.

41

ER Monitoring System

The Brandywine ER configuration consists of seven boreholes with 15 electrodes each for a total of 105 electrodes (see Figure 15 and also Johnson et al., 2014). The borehole electrodes are arranged to optimize imaging of the time-lapse distribution of changes in bulk electrical conductivity caused by the injection, migration, and reaction of the biostimulant.
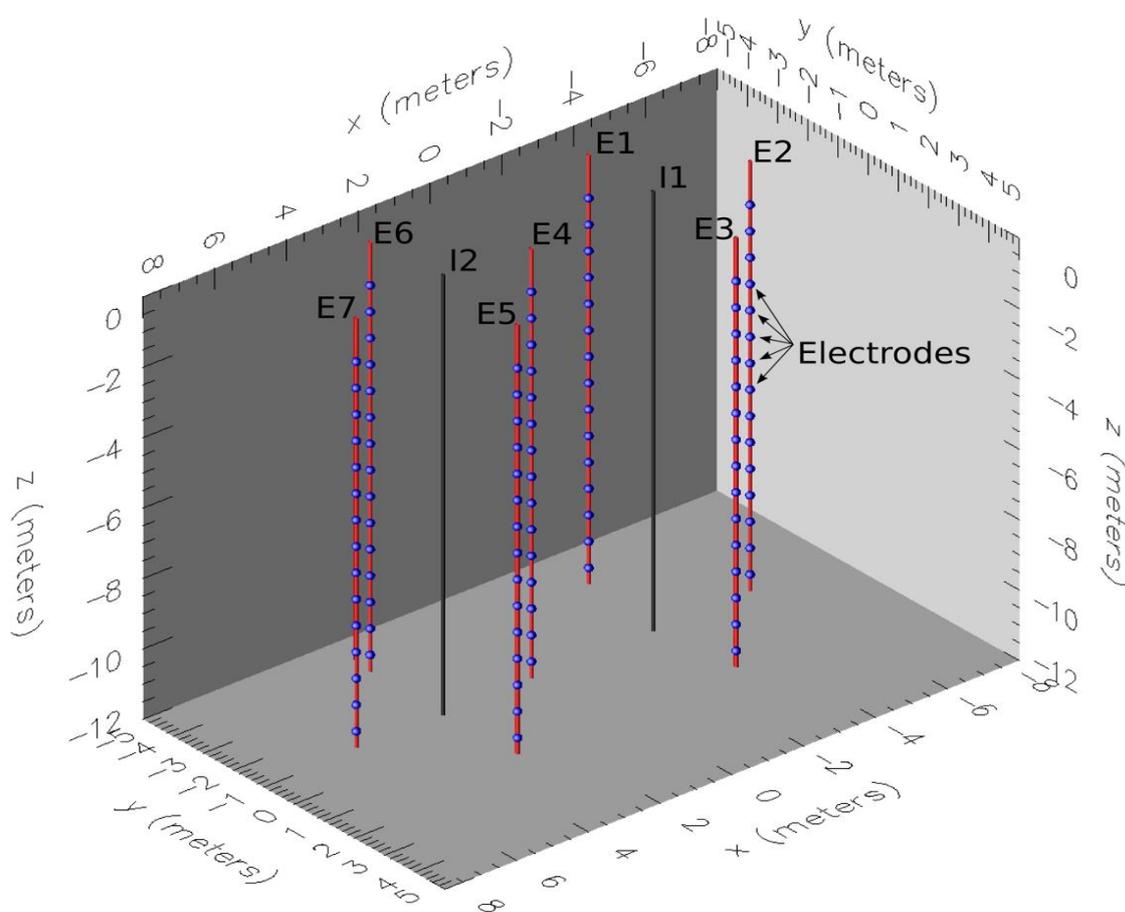

Figure 15 - Configuration of ER boreholes and electrodes at the former Brandywine Defense Reutilization and Marketing Office site, Maryland, USA. Red lines (E1 through E7) represent borehole electrode arrays, blue dots represent electrodes (15 per well), and black lines (I1 and I2) show bioamendment injection locations.

Data Collection and Experimental Design

An [MPT-ER][1]↗ instrument was used to collect 10,939 dipole-dipole measurements in a variety of cross-well and in-well configurations, including full reciprocal measurements (i.e., 21,878 measurements total). The MPT-ER system uses an external voltage source for the current injection electrodes, which was set at 150 V for this survey. Current source and potential measurement electrodes were chosen according to a user-supplied measurement schedule file and switching between electrodes was completed through a control unit and a series of multiplexers attached to the electrode cables. Baseline data sets were collected before amendment injections and equivalent data sets were collected twice daily for approximately three years after injections. The amendment consisted of a proprietary lactate-based bio-stimulant with fluid conductivity significantly greater than groundwater conductivity. Two injections occurred using direct-push methods (i.e., a pipe with an opening at the end is pushed into the subsurface), one at location I1 and one at location I2 in Figure 15. For each injection, the direct-push pipe was advanced to approximately 12 m below ground surface, where approximately 113 L of amendment was injected. The pipe was then retracted by approximately 0.3 m and another 113 L was injected, repeating to approximately 1 m below ground surface. ERT data were not collected during injections but commenced shortly after the injections were completed. Importantly, the amendment formula was modified between injections such that the amendment injected into I1 had greater fluid conductivity than the amendment injected into I2.

Data Quality Control and Assurance

As previously mentioned, data quality is a function of injected current, which depends on the voltage applied to the current electrodes, electrode contact resistance, electrical conductivity of the medium, and distance between electrodes. Data quality is also a function of random and systematic error. As outlined in Section 0, random error can result from a number of factors such as: (1) high geometric factors, which result in a poor signal-to-noise ratio; (2) high contact resistance, which occurs when electrodes are in poor contact with the formation; (3) insufficient (i.e., low relative to what is needed) current injection; and (4) random ambient electrical noise. As discussed in Sections 3.2 and 3.3, random errors can be quantified from stacked and/or reciprocal measurements. It is important to eliminate (or appropriately weight) data with large random errors prior to inversion.

Histograms and summary statistics of the pre-filter reciprocity and apparent resistivity distributions for the Brandywine data are shown in Figure 16. We eliminated data with stacking errors larger than 3 percent, reciprocity larger than 10 percent, or applied

---

[1] Any use of trade, product, or firm names is for descriptive purposes only and does not imply endorsement by the U.S. Government.

currents less than 10 mA. We also eliminated data with apparent resistivities less than zero or greater than 7000 ohm-m, which would well exceed the resistivity expected for saturated medium sands at the site. Apparent resistivities above 7000 ohm-m (71 measurements) make up the tail of the histogram and were assumed to be outliers in this case (Figure 16). This data filtering was performed outside of the inversion software. The editing filters for current, reciprocity, and apparent resistivity removed 90, 58, and 751 measurements, respectively, leaving 10,040 of 10,939 measurements for a total data reduction of approximately 9 percent. Note that this type of data filtering is not required; it is possible to invert datasets with all collected data, especially if weighting each measurement individually by its data error. However, it can be useful to remove particularly poor data—the criteria for which will change with every field system such that the values here should not be assumed to be appropriate at all sites—as there is no need for the model to work to fit them.
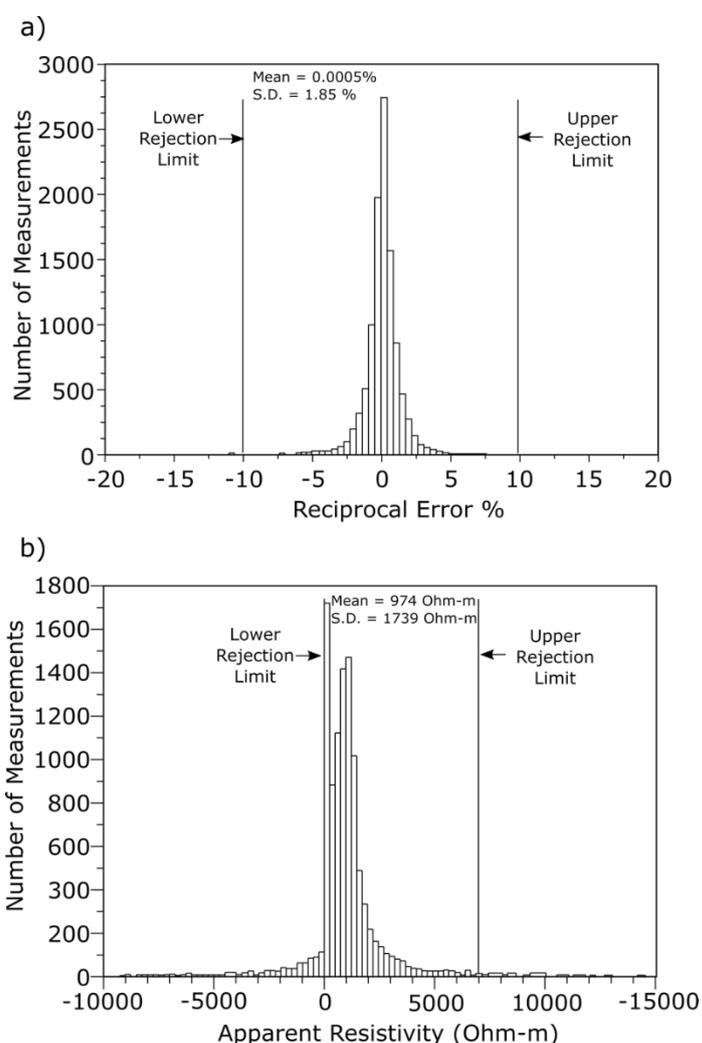

Figure 16 - a) Reciprocal error histogram showing 10 percent data rejection limits and associated statistics. A total of 58 measurements were rejected due to excessive reciprocal error; b) Apparent resistivity histogram and rejection limits. A total of 1316 measurements were rejected due to excessive or negative apparent resistivity.

As discussed in Section 3.3, reciprocal measurements commonly are considered to provide a meaningful quantification of random errors, incorporating instrument error, error arising from nearby anthropogenic current sources, electrical storms, and/or random physical effects in violation of Equation 1 (or Equation 5). Here, however, reciprocal errors are small and have a standard deviation of 1.8 percent (Figure 16a). As shown in the next section, the reciprocal error does not represent the total error (both random and systematic as discussed in Section 4.3) and is inappropriate for use as a stopping criterion in the inversions.

Effect of Data Weighting and Regularization Weighting on Pre-Injection Inversions

Inversions were performed using a 3-D finite-element ER modeling and inversion code (E4D↗) developed at Pacific Northwest National Laboratory. E4D was implemented in parallel to facilitate inversion of large 3D electrical conductivity data sets. However, the Brandywine DRMO data presented here could easily be accommodated by commercially available serial inversion codes on a standard workstation. The principles and effects of data and model weighting (i.e., data noise estimation and regularization) demonstrated here are also valid for commercially available codes.

We stress that for most ER studies, the choices of data weighting and regularization will strongly affect results, and it is critical to experiment with different approaches to help distinguish artifacts from geologic features. Features common to a suite of tomograms inverted from the same dataset with different settings should inspire some degree of confidence for interpretation, whereas features that result only for a specific inversion setting or regularization are more likely to be artifacts. To demonstrate this concept, we inverted the Brandywine data under a variety of choices for data error and regularization. For the base case, we used Equation 11 to estimate data noise with $a = 0.15$ and $b = 0.10$ ohms. This choice was the outcome of trial and error using several different noise estimates, including direct reciprocal errors, and comparing inversion results with one another and with the general geology obtained from core samples. For the base-case regularization, we used an isotropic nearest-neighbor smoothing constraint, whereby neighboring elements are encouraged to be equivalent in bulk conductivity regardless of their orientation with respect to one another. The inversion started with a large ε value, and ε was decreased only when the χ^2 between iterations decreased by less than 5 percent. This constraint and ε 'cooling' procedure was chosen to ensure that any heterogeneity introduced into the inverse solution was required to fit the data (i.e., to ensure a *parsimonious*, or simple, solution).

To demonstrate the effects of stopping criteria on the inversion results, we show examples of inversions with different data misfits in Figure 17 and Figure 18. Note that for most inversion packages, the stopping criteria are based on some measure of data misfit as discussed previously (e.g., RMS or χ^2). Because the stacking and reciprocal errors do not represent the true error (i.e., the error estimated by Equation 11), determination of the

45

appropriate misfit is somewhat subjective. Thus, judgment and prior information are critical for determining an appropriate data fit, as indicated by the amount and distribution of heterogeneity in the inverse solution. For instance, in this case, core samples taken during installation of the ER boreholes indicated an upper layer of fine sands and silts, an intermediate zone of coarse sands and gravels constituting the aquifer, and a lower fine-grained confining unit. The approximate contact depths correspond well to electrical conductivity changes in the 'appropriately' fit tomogram in Figure 17b, suggesting an appropriate data weighting and stopping criteria for this inversion.
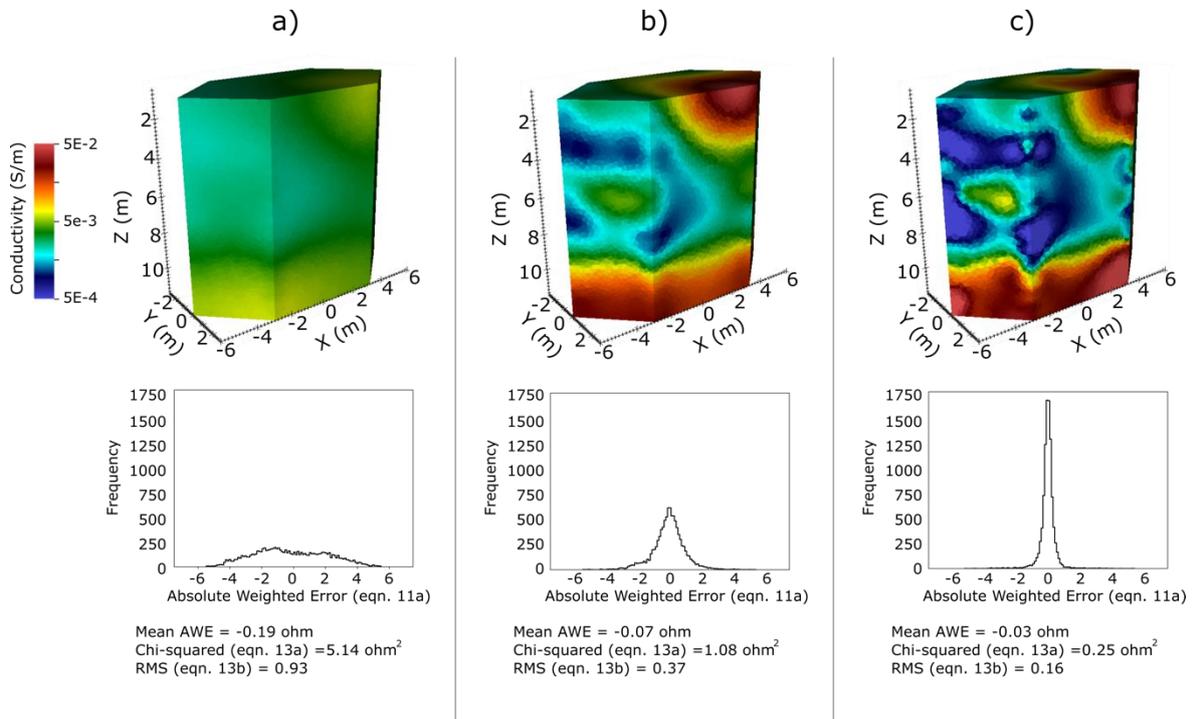
Figure 17 - A demonstration of data overfitting and underfitting. Here the data noise is estimated by Equation 11 using a = 0.15 and b = 0.1 ohm. a) Excessively smooth inverse model due to data underfitting. b) An inverse model with appropriately fit data. c) An inverse model with excessive heterogeneity due to data overfitting.
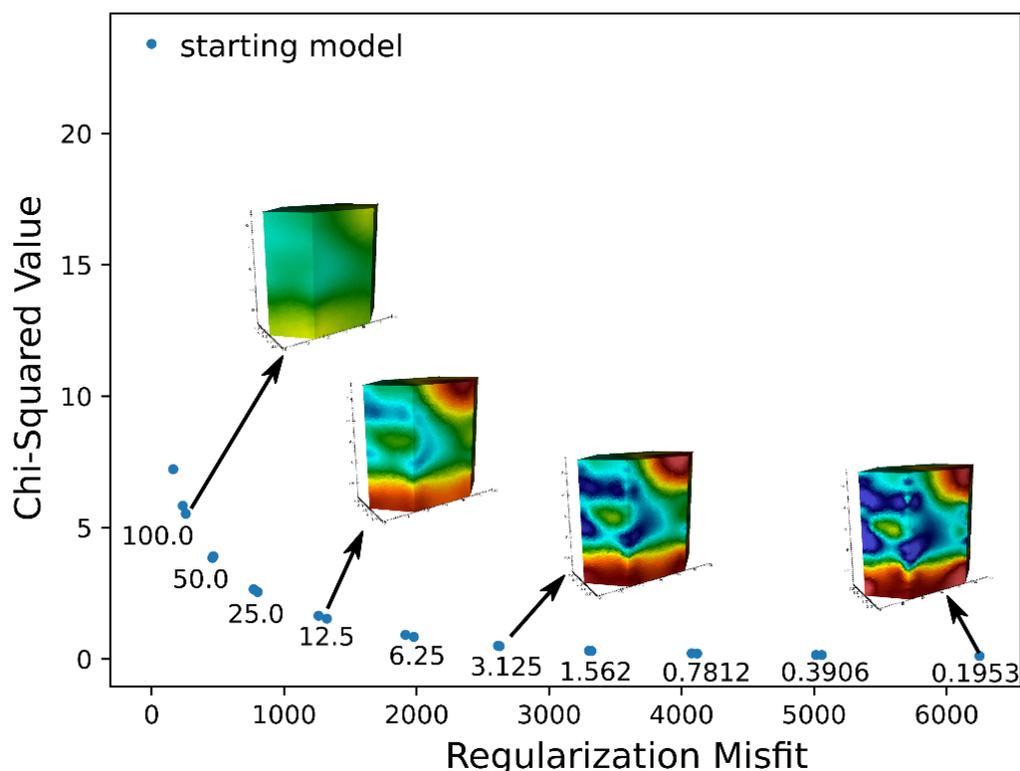
Figure 18 - L-curve plot for the Brandywine inversion. Each point and label on the plot represent an iteration of the inversion and the corresponding regularization weighting value (ε) used for that iteration. As ε decreases, more heterogeneity is introduced into the solution to decrease the χ^2 value, resulting in an increase in the regularization misfit. Representative visualizations of the inverse solution at selected iterations are shown to illustrate model complexity as the inversion progresses.

Figure 18 shows the L-curve representation of the inverse solution. Each point on the L-curve represents an iteration of the inversion, with the regularization term of Equation 9a and b on the horizontal axis and the χ^2 value (data misfit) on the vertical axis. Each point on the L-curve represents a single iteration of the inverse solution. At the homogeneous starting model, the χ^2 value is high, but the regularization misfit is zero. As the inversion progresses, heterogeneity is introduced into the solution to decrease the χ^2 value, causing an increase in the regularization misfit. When the decrease in the χ^2 value is small between iterations (as noted by two points close together on the L-curve), the regularization weighting (i.e., the ε value) is decreased by 50 percent, enabling the inversion to include more heterogeneity and decrease χ^2 at the next iteration. At the tail end of the L-curve, each decrease in ε results in a large increase in heterogeneity, but only a small decrease in the χ^2 value. At this point, it is assumed that the appropriate stopping point has been exceeded and the inversion is fitting noise, thus introducing artifacts into the solution. Given the data error model used in this example, a normalized χ^2 value of 1.08 was reached at ε = 6.25, resulting in the solution shown in Figure 17b.

In addition to stopping criteria, the data weighting scheme can have profound effects on the inversion results. Figure 19 shows two inversions with comparable data misfits [in terms of root-mean-square (RMS) error] but different data weighting schemes.

Figure 19a shows results for the same data weighting scheme and regularization as the inversions in Figure 17b. Figure 19b uses data standard deviations set to a constant value of 0.1 ohm. Other than the data weighting, all inversion parameters for tomograms in Figure 19a and Figure 19b are equal, and the inversion is allowed to iterate to an RMS error of ~0.37. The high χ^2 value in Figure 19b suggests that the constant standard deviation of 0.1 ohm underestimates the true error. That is, fitting the data to a χ^2 value of 1 in this case would overfit the data, cause artifacts, and thus yield less meaningful inversion results. However, the similarity between the tomograms for the same RMS error value suggests that the constant error estimate is useful as a relative data weight in this case.
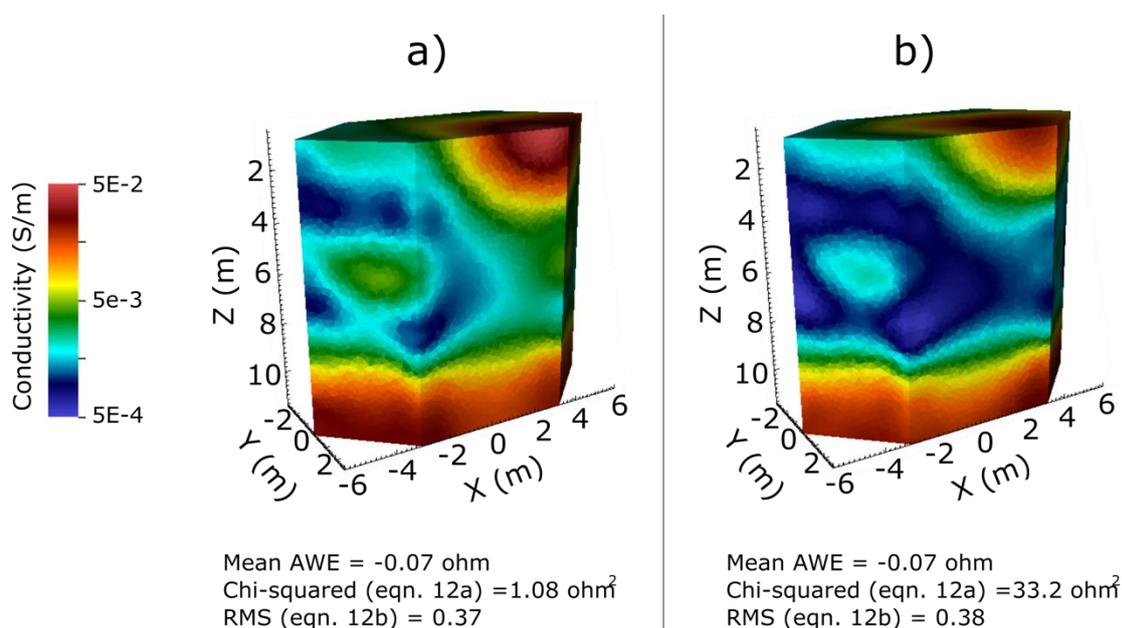

Mean AWE = -0.07 ohm
Chi-squared (eqn. 12a) =1.08 ohm^2
RMS (eqn. 12b) = 0.37

Mean AWE = -0.07 ohm
Chi-squared (eqn. 12a) =33.2 ohm^2
RMS (eqn. 12b) = 0.38

Figure 19 - Effects of data weighting on the inverse solution. a) Data standard deviations are estimated with Equation 11 using $a = 0.15$ and $b = 0.10$. b) Data standard deviations are set to a constant value of 0.10 ohm. Each inversion was fit to approximately the same RMS value (Equation 13b). The χ^2 large value (Equation 13a) of inversion B suggests the data errors used for B underestimate the actual field-based errors. The differences between the inversions in a) and b) are due to the different emphasis placed on different data by the data weighting.

Inverse results also can be affected significantly by the regularization scheme, particularly in cases where the data are noisy and/or the estimated parameters are not well constrained by the data. That is, the effects of regularization are dependent on the ability of the data to resolve the electrical conductivity in all parts of the model, with resolving power varying spatially (e.g., Figure 4). Regularization will have a stronger influence on parts of the model less resolved by the data. To demonstrate the effects of regularization, we show three inversions with different regularization schemes in Figure 20. Although there are significant differences, the major features of the inversion are similar, suggesting these features are relatively well resolved by the data. It is good practice to invert data with several different regularization schemes, as this gives insight into what features are constrained by the data and what features may be controlled by regularization.

48

The GROUNDWATER PROJECT   ©The Authors   Free download from gw-project.org

Anyone may use and share gw-project.org links. Direct distribution of the book is strictly prohibited.

Determination of which inversion features are constrained by the data and which are likely regularization-driven can also be made through *model appraisal*. Most model appraisal approaches require computation of the resolution matrix (Equation 15), which is only feasible for relatively small inverse problems. However, an indication of resolution is given by the sensitivity vector S (Equation 17), which shows the overall sensitivity of each region of the model to the data. The sensitivity vector S for the inverse solution in Figure 17b is shown in Figure 21. Note that the sensitivity is greater near the electrodes and in lower electrical conductivity regions. That is, a change in electrical conductivity in the resistive part of the model will have a greater influence on the data than a change in electrical conductivity in the conductive part.
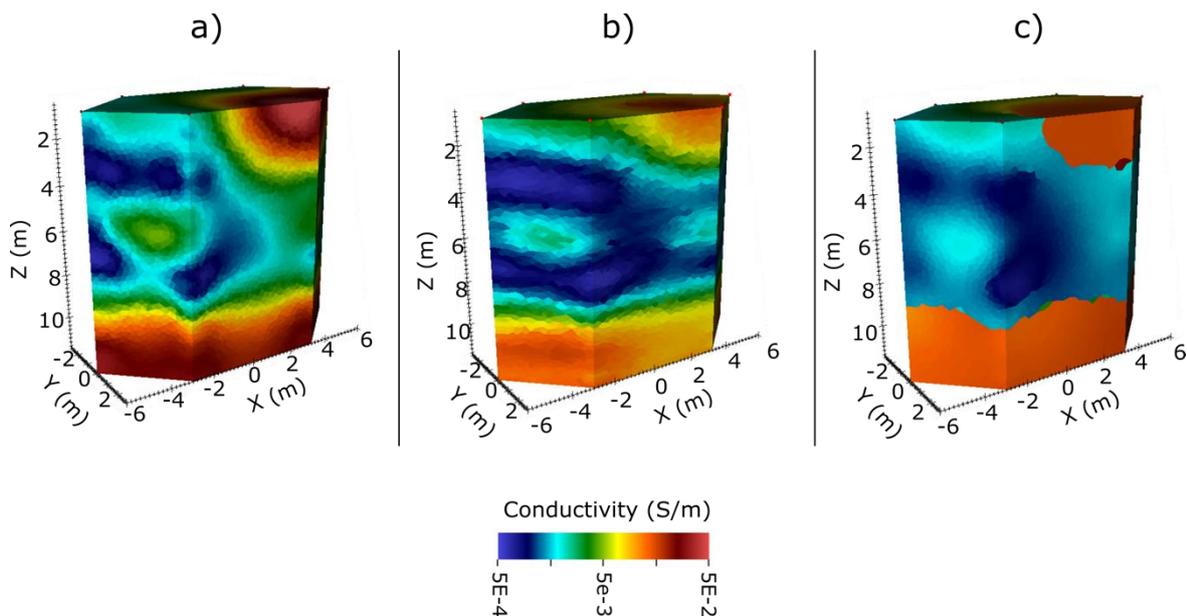
Figure 20 - a) Inverse solution with isotropic nearest-neighbor smoothing constraints. b) Inversion with anisotropic nearest-neighbor smoothing constraints, encouraging homogeneity in the horizontal plane (i.e., layered structure). c) Hybrid regularization that promotes blocky structure at sharp conductivity boundaries. Data were weighted equivalent to the weighting used in Figure 14 and fit to a normalized χ^2 of ~1.0 and an RMS value of ~0.30 in each case.
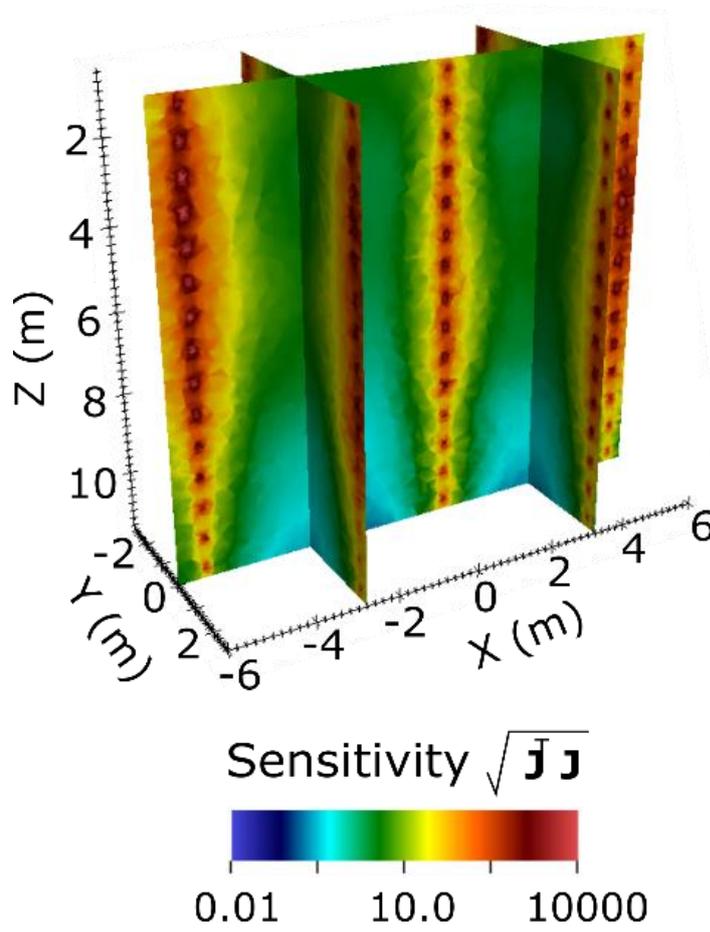
Figure 21 - Cumulative squared sensitivity distribution (S in Equation 17) for the inverse solution in **Figure 17**b. Larger sensitivities are found near electrodes and in lower electrical conductivity regions.

Time-Lapse Inversions

For the time-lapse inversions, the data weighting and convergence criteria for each time-lapse data set were equivalent to that shown in Figure 17b. However, the regularization constraints were modified to encourage temporal changes in bulk conductivity with respect to the baseline inversion (Figure 17b) to vary smoothly in space. To implement those constraints, Equation 18a was added to the regularization constraint matrix, with one equation for each neighboring pair of elements in the computational mesh.

$$\epsilon\left(m_{i,t} - m_{i,ref}\right) = \epsilon\left(m_{j,t} - m_{j,ref}\right) \tag{18a}$$

Here, $m_{i,t}$ is the log conductivity of computational mesh element i at time t, $m_{j,t}$ is a neighboring element, $m_{i,ref}$ represents the pre-injection, baseline log conductivity of element i, and ϵ represents the regularization weighting parameter. Noting that:

$$m_{i,t} = m_{i,t-1} + \Delta m_{i,t} \tag{18b}$$

(and similarly for $m_{j,t}$) Equation 18a can be re-arranged and written as Equation 18c.

$$\epsilon\left(\Delta m_{i,t} - \Delta m_{j,t}\right) = \epsilon\left(m_{i,ref} - m_{j,ref} + m_{i,t-1} - m_{j,t-1}\right) \tag{18c}$$

The left- and right-hand side of Equation 18c are incorporated into the matrix equations in the left- and right-hand sides of the inversion formulation in Equation 10a, respectively.

Figure 22 shows four representative examples of the time-lapse inversion results spanning approximately one year. The elevated fluid conductivity of the amendment injected at I1 compared to I2 is immediately evident on day 5, as the increase in bulk conductivity at I1 is greater than at I2. Over time, the amendment plume spreads laterally, which is important for effective coverage and treatment. After day 93, the plume sinks and spreads over the lower flow-bounding unit, likely due to density-driven flow. By day 371, the plume is diluted relative to day 93, as expressed by a decrease in bulk conductivity.
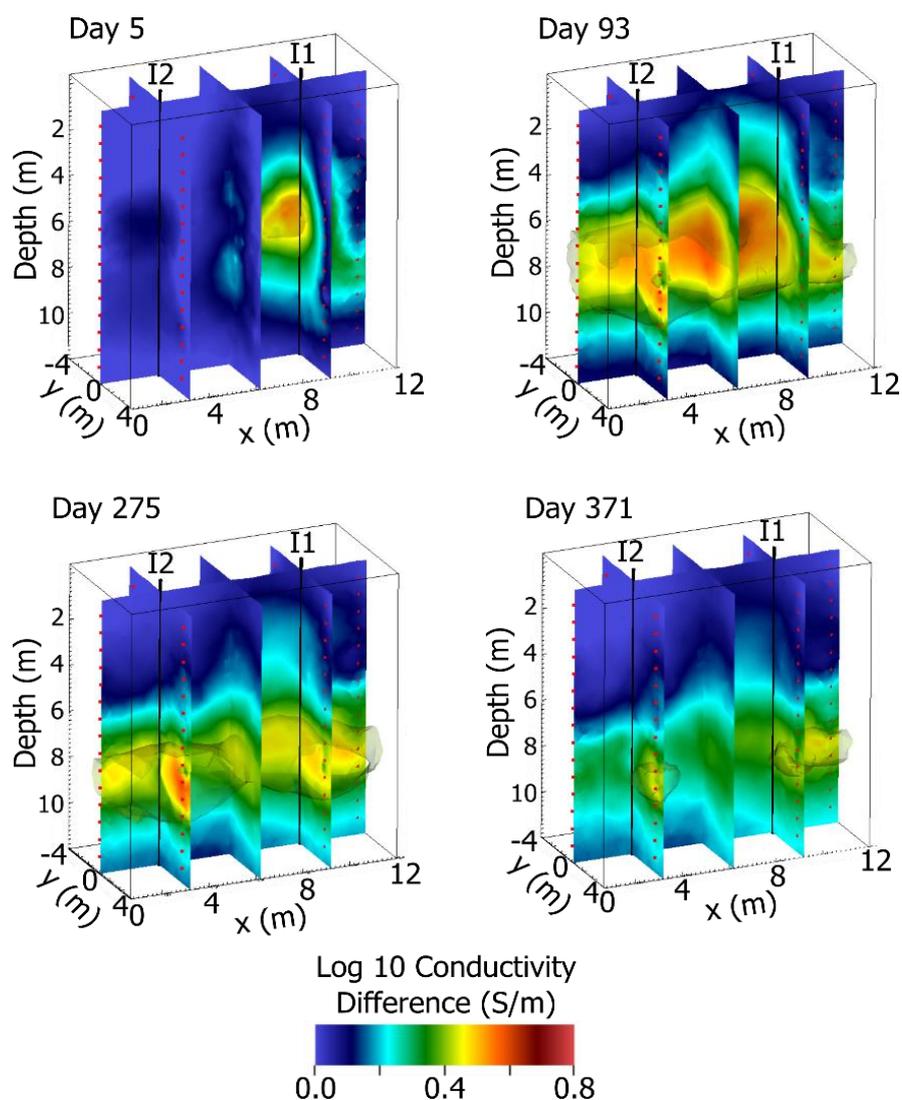
Figure 22 - Example time-lapse inversions showing the changes in bulk conductivity caused by the presence of amendment. After injection, the amendment experienced density-driven downward flow and lateral flow over the lower bounding unit contact at approximately 10 m depth (Figure 17b). The progression from day 93 to day 371 shows the plume sinking and diluting.

6   Overview and Future Directions

Instrumentation and software for electrical imaging are evolving rapidly, as are the applications to hydrogeology. Advances in multi-channel systems now allow for the collection of large 3-D datasets from systems involving hundreds of electrodes, and advances in computing and inversion software allow analysis of such datasets on desktop computers, which opens up possibilities for these methods to be used in more hydrogeologic systems.

Despite these advances, experimental design and effective data analysis require considerable care and scientific insight to ensure meaningful results and interpretation for hydrogeologic processes and parameters. Practitioners are faced with numerous choices for hardware settings (e.g., stacking error cutoffs, applied current, pulse duration) and inversion settings (e.g., regularization, measurement weights), many of which can strongly affect reconstructed images. In cases where quantitative information is to be extracted from tomograms (i.e., rock physics models are applied to tomograms, estimation of hydrologic or geochemical processes changing through time), careful selection of inversion parameters is critical. Data overfitting can result in spurious structures and unrealistic estimates of geophysical and, thus, unrealistic hydrogeologic parameters of interest. On the other hand, data underfitting may result in tomograms that underpredict the degree of spatial variability and, thus, the variability of hydrogeologic parameters. Although multiple strategies to prevent overfitting and underfitting (e.g., L-curve, Occam inversion, and GCV) are discussed in the literature, application of these techniques is less common in practice and not supported by all commercially available electrical imaging inversion software. Because inversion settings can strongly affect resulting tomograms, it is important to document and justify choices. Without such documentation, reproduction of results is problematic.

The goal of this book is to demonstrate and document best practices for electrical imaging data collection and analysis for hydrogeology students and practitioners. In summary, we provide guidelines in seven areas:

1) <u>Survey geometry design:</u> Numerical modeling, i.e., synthetic experiments or 'pre modeling' (e.g., Terry et al., 2017), should be employed prior to collecting geophysical field data to determine the best survey geometry, based on a best estimate of subsurface heterogeneity or processes of interest and the amount of time available to collect data (a particular issue when monitoring time-lapse processes, where temporal smearing will need to be minimized). Note that the maximum offset between electrodes is limited by the power of the electrical imaging unit and the unit's ability to inject sufficient current to achieve a good signal-to-noise ratio. Good quadripoles can be selected, in part, by choosing geometries where the geometric factor is small. If boreholes are to be used, they should be spaced such that electrode strings are at least 1.5 times as long

52

vertically as their horizontal separation distance. Survey geometries should capitalize on the sensitivity of each measurement and maximize the coverage of the tomogram.

2) <u>Standard procedures for data collection:</u> Data collection and quality assurance and control should be documented using standardized forms and procedures that include how field equipment was set up and deployed, electrode locations, how errors and topography were measured in the field, weather, battery voltages, filenames, contact resistances and the locations of any infrastructure that could influence the measurements.

3) <u>Quantification of measurement error:</u> Stacked (at minimum), reciprocal, and/or repeated errors should be collected in the field to assess the quality of the data, inform the editing of datasets, and calculate minimum measurement weights for the inversion.

4) <u>Selection of inversion parameters:</u> Existing data and (hydro)geologic insight should be used to inform selection of inversion parameters or to develop prior information to inform the inversion process, like imposing known layers or contacts. For 2-D datasets involving multiple planes, it is useful to apply multiple approaches to data from one plane, compare results, and design a consistent approach to inversion for data from across the site. Investigation of alternative inversion settings can aid in distinguishing artifacts from hydrogeologic features.

5) <u>Checks on inversion results:</u> Tomograms should be evaluated for likely inversion artifacts and the effects of bad data. The practitioner should look at the range of estimated electrical conductivity values for plausibility; pixelated (checkerboard) appearance of tomograms; artifacts such as streaking, anomalous blocks, or diagonal patterns; and goodness of fit and convergence of the inversion.

6) <u>Resolution assessment:</u> Results of tomograms should be compared with the sensitivity and/or resolution matrix to assess the general quality of the tomogram.

7) <u>Comparison to other information:</u> Tomograms and our interpretations of them should be considered given existing information, including hydrogeologic maps, lithology, borehole logs, hydraulic tests, and even tables of expected properties (given the wealth of published ER and IP data that exist for both unconsolidated and consolidated materials). Borehole logs can provide information to help interpret features seen in tomograms and to help correlate estimated electrical properties with lithology and/or hydraulic properties.

7   Exercises

Exercise 1

Describe the difference between resistivity and resistance. How is apparent resistivity different than both resistivity and resistance?

Click for solution to exercise 1⤵

Exercise 2

Examine the mathematical parallels between Darcy's law and Ohm's law.

Click for solution to exercise 2⤵

Exercise 3

Select and describe the hydrologic equivalent of a:
a. Dead battery?
b. Short circuit?
c. Open circuit?
d. Voltmeter?

Click for solution to exercise 3⤵

Exercise 4

Sketch the field layout for a 1D resistivity sounding, showing how electrodes are placed and moved to vary survey depth.

Click for solution to exercise 4⤵

Exercise 5

Calculate the apparent resistivity in the following arbitrary electrode configuration when a 5 mA current is injected between electrodes A and B and 80 mV is measured between M and N.
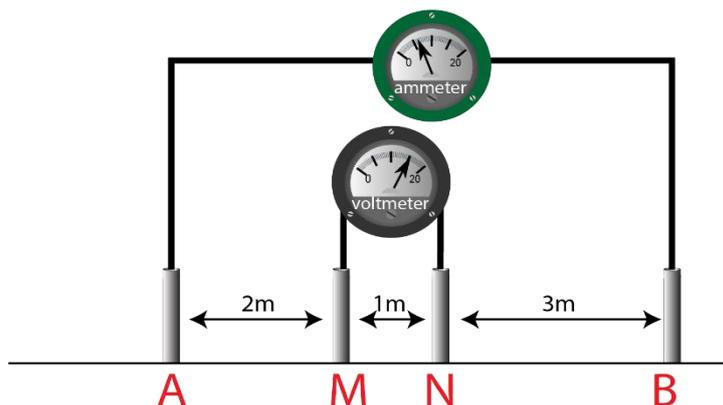
Click for solution to exercise 5⤵

Exercise 6

Calculate the geometric factors, measured voltage differences and signal-to-noise ratio (SNR, the ratio of the field measured voltage difference to the noise) for a Wenner and dipole-dipole array based on the information given (fill out the table below).

Current injected [I]: 2 mA

Apparent resistivity [ρ]: 250 ohm-m

Noise level: 15 mV

Array	a(m)	n	K_g	V(mV)	SNR
Wenner	5	-			
Dipole-dipole	3	3			

Click for solution to exercise 6⤵

Exercise 7

Explain, with the help of an illustration, how the ER inversion process works. Highlight [1] the starting model, [2] the field data, and [3] the decision to update the model.

Click for solution to exercise 7⤵

Exercise 8

Hypothesize how the map of inverted conductivity of the earth below an array of electrodes is likely to deviate from reality. Explain factors that cause this deviation.

Click for solution to exercise 8⤵

8   References

Barker, R.D, 1989, Depth of investigation of collinear symmetrical four-electrode arrays. Geophysics, volume 54, pages 1031-1037, doi: 10.1190/1.1442728↗.

Binley, A., G. Cassiani, R. Middleton, and P. Winship, 2002, Vadose zone flow model parameterization using cross-borehole radar and resistivity imaging. Journal of Hydrology, volume 267, pages 147-159, doi: 10.1016/S0022-1694(02)00146-4↗.

Binley, A., A. Ramirez, and W. Daily, 1995, Regularized image reconstruction of noisy electrical resistance tomography data, *in* Proceedings of the 4th Workshop of the European Concerted Action on Process Tomography, editors, M.S. Beck et al., Bergen, Norway, pages 401-410.

Binley, A. and L. Slater, 2020, Resistivity and Induced Polarization: Theory and Applications to the Near-Surface Earth. Cambridge University Press, 408 pages, ISBN 9781108492744.

Blanchy, G., S. Saneiyan, J. Boyd, P. McLachlan and A. Binley, 2020, ResIPy, an intuitive open-source software for complex geoelectrical inversion/modeling. Computers & Geosciences, volume 137, page 104423, doi: 10.1016/j.cageo.2020.104423↗.

Caterina, D., T. Hermans and F. Nguyen, 2014, Case studies of incorporation of prior information in electrical resistivity tomography: comparison of different approaches. Near Surface Geophysics, volume 12, issue 4, pages 451-465, doi: 10.3997/1873-0604.2013070↗.

Claerbout, J.F. and F. Muir, 1973, Robust modeling with erratic data. Geophysics, volume 38, issue 5, pages 826–844, doi: 10.1190/1.1440378↗.

Cockett, R., S. Kang, L.J. Heagy, A. Pidlisecky and D.W. Oldenburg, 2015, SimPEG: An open-source framework for simulation and gradient based parameter estimation in geophysical applications. Computers & Geosciences, volume 85, part A, pages 142-154, doi: 10.1016/j.cageo.2015.09.015↗.

Constable, S.C., R.L. Parker and C.G. Constable, 1987, Occam's inversion: a practical algorithm for generating smooth models from electromagnetic sounding data. Geophysics, volume 52, issue 3, pages 289-300, doi: 10.1190/1.1442303↗.

Dahlin, T. and V. Leroux, 2012, Improvement in time-domain induced polarization data quality with multi-electrode systems by separating current and potential cables. Near Surface Geophysics, volume 10, issue 6, pages 545-565, doi: 10.3997/1873-0604.2012028↗.

Dahlin, T. and M.H. Loke, 2015, Negative apparent chargeability in time-domain induced polarization data. Journal of Applied Geophysics, volume 123, pages 322-332, doi: 10.1016/j.jappgeo.2015.08.012↗.

Daily, W., and E. Owen, 1991, Cross-borehole resistivity tomography. Geophysics, volume 56, number 8, pages 1228-1235, doi: 10.1190/1.1443142↗.

Daily, W. and A. Ramirez, 1995, Electrical resistance tomography during in-situ trichloroethylene remediation at the Savannah River Site. Journal of Applied Geophysics, volume 33, issue 4, pages 239-249, doi: 10.1016/0926-9851(95)90044-6↗.

Day-Lewis, F.D., Y. Chen, and K. Singha, 2007, Moment inference from tomograms. Geophysical Research Letters, volume 34, issue 22, doi: 10.1029/2007GL031621↗.

Day-Lewis, F.D., J.W. Lane Jr., J.M. Harris, and S.M. Gorelick, 2003, Time-lapse imaging of saline tracer tests using cross-borehole radar tomography. Water Resources Research, volume 39, issue 10, page 1290, doi:10.1029/2002WR001722↗.

Day-Lewis, F.D., K. Singha, and A.M. Binley, 2005, Applying petrophysical models to radar traveltime and electrical resistivity tomograms – Resolution-dependent limitations. Journal of Geophysical Research, volume 110, issue B8, doi:10.1029/2004JB003569↗.

Day-Lewis, F.D., L.D. Slater, J. Robinson, C.D. Johnson, N. Terry, and D. Werkema, 2017, An overview of geophysical technologies appropriate for characterization and monitoring at fractured-rock sites. Journal of Environmental Management, volume 204, pages 709-720, doi: 10.1016/j.jenvman.2017.04.033↗.

Day-Lewis, F.D., E.A. White, C.D. Johnson, J.W. Lane Jr., and M. Belaval, 2006, Continuous resistivity profiling to delineate submarine groundwater discharge—Examples and limitations. The Leading Edge, volume 25, issue 6, pages 724-728, doi: 10.1190/1.2210056↗.

Dey, A., and H.F. Morrison, 1979, Resistivity modeling for arbitrarily shaped three-dimensional structures. Geophysics, volume 44, issue 4, pages 753-780, doi: 10.1190/1.1440975↗.

Farquharson, C.G. and D.W. Oldenburg, 1998, Non-linear inversion using general measures of data misfit and model structure. Geophysical Journal International, volume 134, issue 1, pages 213-227, doi: 10.1046/j.1365-246x.1998.00555.x↗.

Farquharson, C.G., and D.W. Oldenburg, 2004, A comparison of automatic techniques for estimating the regularization parameter in non-linear inverse problems. Geophysical Journal International, volume 156, issue 3, pages 411-425, doi: 10.1111/j.1365-246X.2004.02190.x↗.

Flores Orozco, A., J. Gallistl, M. Bücker and K.H. Williams, 2018, Decay curve analysis for data error quantification in time-domain induced polarization imaging. Geophysics, volume 83, issue 2, pages 1MA-Z8, doi: 10.1190/geo2016-0714.1↗.

Freeze, R.A. and J.A. Cherry, 1979, Groundwater. Prentice Hall, pages 360-364, 604, https://gw-project.org/books/groundwater/↗.

Gouveia, W.P. and J.A. Scales, 1997, Resolution of seismic waveform inversion–Bayes versus Occam. Inverse Problems, volume 13, pages 322-349, https://iopscience.iop.org/article/10.1088/0266-5611/13/2/009/meta↗.

Griffiths, D.H., J. Turnbull, and A.I. Olayinka, 1990, Two-dimensional resistivity mapping with a computer-controlled array. First Break, volume 8, issue 4, pages 121–129, doi: 10.3997/1365-2397.1990008↗.

Haber, E. and D. Oldenburg, 2000, A GCV based method for nonlinear ill-posed problems. Computational Geosciences, volume 4, pages 41-63, doi: 10.1023/A:1011599530422↗.

Hallof, P.G., 1957, On the interpretation of resistivity and induced polarization measurements. Doctor of Philosophy Dissertation, Massachusetts Institute of Technology, http://hdl.handle.net/1721.1/54400↗.

Hansen, P.C., and D.P. O'Leary, 1993, The use of the L-curve in the regularization of discrete ill-posed problems. Society for Industrial and Applied Mathematics (SIAM) Journal of Scientific Computing, volume 14, issue 6, pages 1487-1503, doi: 10.1137/0914086↗.

Hermans, T., A. Kemna and F. Nguyen, 2016, Covariance-constrained difference inversion of time-lapse electrical resistivity tomography data. Geophysics, volume 81, issue 5, pages 311-E322, doi: 10.1190/geo2015-0491.1#.

Hördt, A., P. Weidelt and A. Przyklenk, 2013, Contact impedance of grounded and capacitive electrodes. Geophysical Journal International, volume 193, issue 1, pages 187-196, doi: 10.1093/gji/ggs091↗.

Johnson, T.C., R.J. Versteeg, A. Ward, F.D. Day-Lewis, and A. Revil, 2010, Improved hydrogeophysical characterization and monitoring through parallel modeling and inversion of time-domain resistivity and induced polarization data. Geophysics, volume 75, issue 4, pages 1JA-Z98, doi: 10.1190/1.3475513↗.

Johnson, T.C., R.J. Versteeg, F.D. Day-Lewis, W. Major, and J.W. Lane Jr., 2014, Time-lapse electrical geophysical monitoring of amendment-based biostimulation. Groundwater, volume 53, issue 6, pages 920-932, doi: 10.1111/gwat.12291↗.

Jung, H. K., D.J. Min, H.S. Lee, S. Oh, and H. Chung, 2009. Negative apparent resistivity in dipole-dipole electrical surveys. Exploration Geophysics, volume 40, issue 1, pages 33-40, doi: 10.1071/EG08111↗.

Kitanidis, P.K., 1997, The minimum structure solution to the inverse problem. Water Resources Research, volume 33, issue 10, pages 2263-2272, doi: 10.1029/97WR01619↗.

LaBrecque, D. and W. Daily, 2008, Assessment of measurement errors for galvanic-resistivity electrodes of different composition. Geophysics, volume 73, issue 2, pages 1MA-Z29, https://doi.org/10.1190/1.2823457↗.

LaBrecque, D.J., M. Miletto, W. Daily, A. Ramirez, and E. Owen, 1996, The effects of noise on Occam's inversion of resistivity tomography data. Geophysics, volume 61, issue 2, pages 538-548, doi: 10.1190/1.1443980↗.

LaBrecque D.J., X. Yang, 2001, Difference inversion of ERT Data: A fast inversion method for 3-D in situ monitoring. Journal of Environmental and Engineering Geophysics, volume 6, issue 2, pages 83–89, doi: 10.4133/JEEG6.2.83↗.

Lesparre, N., F. Nguyen, A Kemna, T. Robert, T Hermans, M. Daoudi, and A. Flores Orozco, 2017, A new approach for time-lapse data weighting in ERT. Geophysics, volume 82, issue 6, pages 325-E333, doi: 10.1190/geo2017-0024.1↗.

Linde, N, 2014, Falsification and corroboration of conceptual hydrological models using geophysical data. WIREs Water, volume 1, pages 151-171. doi: 10.1002/wat2.1011↗.

Loke, M.H., R.I. Acworth, and T. Dahlin, 2003, A comparison of smooth and blocky inversion methods in 2D electrical imaging surveys. Exploration Geophysics, volume 34, pages 182-187, doi: 10.1071/EG03182↗.

Loke, M.H. and R.D. Barker, 1996, Rapid least-squares inversion of apparent resistivity pseudosections by a quasi-Newton method. Geophysical Prospecting, volume 44, issue 1, pages 131–152, doi: j.1365-2478.1996.tb00142.x↗.

Luo, Y. and G. Zhang, 1998, Forward Theory of Spectral Induced Polarization, *in* Theory and Application of Spectral Induced Polarization. Society of Exploration Geophysicists, volume 2, pages 13-90, doi: 10.1190/1.9781560801856.ch2↗.

Lytle, R.J. and K.A. Dines, 1978, Impedance camera: A system for determining the spatial variation of electrical conductivity, Report No. UCRL-52413. Lawrence Livermore Lab., page 11, https://www.osti.gov/servlets/purl/6753686↗.

Menke, W., 1984, The resolving power of cross-borehole tomography: Geophysical Research Letters, volume 11, issue 2, pages 105-108, doi: 10.1029/GL011i002p00105↗.

Morris, G., A.M. Binley, and R.D. Ogilvy, 2004, Comparison of different electrode materials for induced polarization measurements. Symposium on the Application of Geophysics to Environmental & Engineering Problems (SAGEEP2004), volume 17, pages 573, doi: 10.4133/1.2923371↗.

Mwakanyamale, K., L. Slater, A. Binley, and D. Ntarlagiannis, 2012, Lithologic imaging using complex conductivity: Lessons learned from the Hanford 300 Area. Geophysics, volume 77, issue 6, pages E397-E409, doi: 10.1190/geo2011-0407.1↗.

Nguyen, F., A. Kemna, T. Robert, and T. Hermans, 2016, Data-driven selection of the minimum-gradient support parameter in time-lapse focused electrical imaging. Geophysics, volume 81, issue 1, pages 1JF-Z7, https://doi.org/10.1190/geo2015-0226.1↗.

Oldenburg, D.W. and Y. Li, 1999, Estimating depth of investigation in dc resistivity and IP surveys. Geophysics, volume 64, issue 2, pages 403–416, doi: 10.1190/1.1444545↗.

Pidlisecky, A., E. Haber, and R. Knight, 2007, RESINVM3D: A MATLAB 3-D Resistivity Inversion Package, Geophysics, volume 72, issue 2, pages H1-H10, doi: 10.1190/1.2402499↗.

Roy, A. and A. Apparao, 1971, Depth of investigation in direct current methods. Geophysics, volume 36, issue 5, pages 943-959, doi: 10.1190/1.1440226↗.

Rücker, C. and T. Günther, 2011, The simulation of finite ERT electrodes using the complete electrode model. Geophysics, volume 76, issue 4, pages 1JA-Z99, doi: 10.1190/1.3581356↗.

Rücker, C., T. Günther, and F.M. Wagner, 2017, pyGIMLi: An open-source library for modelling and inversion in geophysics. Computers & Geosciences, volume 109, pages 106-123, doi: 10.1016/j.cageo.2017.07.011↗.

Singha, K., F.D. Day-Lewis, T. Johnson and L.D. Slater, 2014, Advances in interpretation of subsurface processes with time-lapse electrical imaging. Hydrological Processes, page 28. doi: 10.1002/hyp.10280↗.

Singha, K. and S.M. Gorelick, 2005, Saline tracer visualized with electrical resistivity tomography–Field scale moment analysis: Water Resources Research, volume 41, W05023, doi: 10.1029/2004WR003460↗.

Slater, L., 2007, Near surface electrical characterization of hydraulic conductivity: from petrophysical properties to aquifer geometries - a review, Surveys in Geophysics, volume 28, pages 169-197.

Slater, L., A.M. Binley, W. Daily and R. Johnson, 2000, Cross-hole electrical imaging of a controlled saline tracer injection. Journal of Applied Geophysics, volume 44, issues 2-3, pages 85-102, doi: 10.1016/S0926-9851(00)00002-1↗.

Slater, L. and A. Binley, 2006, Synthetic and field-based electrical imaging of a zerovalent iron barrier: Implications for monitoring long-term barrier performance. Geophysics, volume 71, issue 5, pages 1SO-viii, doi: 10.1190/1.2235931↗.

Slater, L.D. and D. Lesmes, 2002, IP interpretation in environmental investigations. Geophysics, volume 67, issue 1, pages 77-88, doi: 10.1190/1.1451353↗.

Slater, L.D., D. Ntarlagiannis, F.D. Day-Lewis, K. Mwakanyamale, R.J. Versteeg, A. Ward, C. Strickland, C.D. Johnson, and J.W. Lane Jr., 2010, Use of electrical imaging and distributed temperature sensing methods to characterize surface water–groundwater exchange regulating uranium transport at the Hanford 300 Area, Washington. Water Resources Research, volume 46, issue 10, doi: 10.1029/2010WR009110↗.

Stummer, P., H. Maurer, and A.G. Green, 2004, Experimental design – Electrical resistivity datasets that provide optimum subsurface information. Geophysics, volume 69, issue 1, doi:10.1190/1.1649381↗.

Sumner, J.S., 1976, Principles of Induced Polarization for Geophysical Exploration. Elsevier, New York, page 277, ISBN 9780444599872.

Tarantola, A., 1987, Inverse problem theory – Methods for data fitting and model parameter estimation. Elsevier, Amsterdam, page 613, ISBN 978-0444427656.

Terry, N., F.D. Day-Lewis, J.L. Robinson, L.D. Slater, K. Halford, A. Binley, J.W. Lane, and D. Werkema, 2017, Scenario evaluator for electrical resistivity survey pre-modeling tool. Groundwater, volume 55, issue 6, pages 885-890, doi: 10.1111/gwat.12522↗.

Tikhonov, A.N. and V.Y. Arsenin, 1977, Solutions of ill-posed problems. John Wiley & Sons, New York, page 258, ISBN 978-0470991244.

Tripp, A.C., G.W. Hohmann, and C.M. Swift Jr., 1984, Two-dimensional resistivity inversion. Geophysics, volume 49, issue 10, pages 1708-1717, doi: 10.1190/1.1441578↗.

United States Air Force, 2006, Interim Record of Decision, Site SS-01, Brandywine DRMO Andrews Air Force Base, Maryland, page 112.

Vasco, D.W., A. Datta-Gupta, and J.C.S. Long, 1997, Resolution and uncertainty in hydrologic characterization. Water Resources Research, volume 33, issue 3, pages 379-397, doi: 10.1029/96WR03301↗.

Wang, C., A. Binley, L.D. Slater, 2020, On negative induced polarization in frequency domain measurements. Geophysical Journal International, volume 225, issue 1, pages 342-353, doi: 10.1093/gji/ggaa581↗.

Wilkinson, P. B., J.E. Chambers, M. Lelliott, G.P. Wealthall, and R.D. Ogilvy, 2008, Extreme sensitivity of crosshole electrical resistivity tomography measurements to geometric errors. Geophysical Journal International, volume 173, issue 1, pages 49-62, doi: 10.1111/j.1365-246X.2008.03725.x↗.

Xu, B. and M. Noel, 1993, On the completeness of data sets with multielectrode systems for electrical resistivity survey. Geophysical Prospecting, volume 41, issue 6, pages 791-801, doi: 10.1111/j.1365-2478.1993.tb00885.x↗.

Zarif, F., P. Kessouri, and L. Slater, 2017, Recommendations for field-scale induced polarization (IP) data acquisition and interpretation. Journal of Environmental and Engineering Geophysics, volume 22, issue 4, pages 395-410, doi: 10.2113/JEEG22.4.395↗.

Zhody, A.A.R., G.P. Eaton, and D.R. Mabey, 1974, Application of surface geophysics to ground-water investigations. U.S. Geological Survey Techniques of Water-Resources Investigations, book 2, chapter D1, page 86, https://pubs.usgs.gov/twri/twri2-d1/↗.

9 Boxes

Box 1 Scenario Evaluator for Electrical Resistivity (SEER)

As discussed in Section 2, synthetic modeling provides useful insight for 1) designing geophysical surveys, and 2) understanding the ability of a given survey to resolve a hypothetical target. Synthetic modeling provides a basis for 'go/no-go' decisions on geophysical field campaigns, i.e., whether a survey can adequately resolve expected targets so is worth the expense. Many public-domain and commercially available off-the-shelf software packages for electrical imaging provide synthetic modeling capabilities. In this exercise, we consider the public-domain tool SEER, the Scenario Evaluator for Electrical Resistivity. Available for free from the U.S. Geological Survey, SEER is a spreadsheet-based tool for synthetic modeling of resistivity experiments. SEER is user friendly but limited in its functionality.

To get started with the SEER software, proceed through the steps described in the following bullets, then set up a simple model as described and continue with the activities.

- Download the zip file containing SEER from the USGS repository at https://doi.org/10.5066/F7028PQ1↗. The README file on the web page provides a brief overview and background information about the software.

- Extract the contents of the zip file into a folder on your computer. This will produce the SEER.xlsm spreadsheet, the SEERhelp.chm file which is an electronic user's manual that can be accessed by double clicking on the file, and a folder titled "ResponseArrays" that contains the results of previously executed simulations. There is also an instructional video↗ that describes electrical resistivity imaging and explains how SEER can be useful to designing electrical resistivity surveys.

- Open the spreadsheet. You will need to enable macros when requested to do so by Excel. After reading the INTRO worksheet, navigate to the "Survey" worksheet. There are four template models available from the Scenario drop-down menu in cell B1 of the worksheet. These include 1) DNAPL pool, 2) LNAPL pool, 3) underground storage tank (UST), and 4) block targets (BLOCKS); these can all be modified by the user. In cells B4 through B7, the user may adjust survey parameters including the number of electrodes, type of survey, measurement error levels, and whether borehole electrodes will be used. Familiarize yourself with the operation of the spreadsheet and the three template models, by making selections and clicking the "Simulate" button.

To explore how to make a custom model by selecting a template and modifying the parameters. Begin by selecting the UST template model. Starting from this template of a layered system, you can create a homogeneous background. Be sure to unclick the 'Using specified scenario checkbox' to enable a custom model. You will assess the ability of electrical imaging to resolve a water filled cavity. Change the background for the UST

62

The GROUNDWATER PROJECT ©The Authors Free download from gw-project.org

Anyone may use and share gw-project.org links. Direct distribution of the book is strictly prohibited.

model to 500 ohm-m. Assume 1-m electrode spacing, 10% measurement error, and a dipole-dipole survey. Next. explore what you can do with the SEER software through the following activities.

Activity 1) Assume the electrical conductivity of the water-filled cavity is 200 micro-S/cm. Convert the fluid conductivity to resistivity for input to the spreadsheet. (Hint: resistivity is the reciprocal of conductivity, and 10 S is equivalent to 0.1 ohms.)

Activity 2) Assume the cavity occupies the space from cells in columns AL to AO and rows 13 to 15, and assign the resistivity you calculated to these cells. Press the 'Simulate' button and the spreadsheet will produce the predicted inversion result for your hypothetical model. Evaluate how well your predicted inversion result compares to your true cavity model. Consider its resolution of the top, sides, and bottom of the cavity, as well as how well the estimated resistivity compares to the true resistivity.

Activity 3) Explore how changing the measurement error to 1% and pressing the 'Simulate' button changes the result.

Activity 4) Explore how changing the survey type to 'Combined' and pressing the 'Simulate' button changes the result.

Activity 5) Explore how adding borehole electrodes and pressing the 'Simulate' button changes the result.

Having gained familiarity with how to change both subsurface properties and survey parameters, we encourage you to explore other subsurface systems and combinations of survey configurations. Given the level of importance of precisely defining subsurface properties for a given project, simulating the resistivity survey before undertaking the field work provides the information needed to design the field survey by balancing the cost of conducting the survey against the expected resolution in the result. Of course, one needs to have an estimate of the size, depth, and relative resistivity of the features of interest.

63

Solution to Activity 1

To calculate the cavity resistivity based on the conductivity of 200 micro-S/cm, first convert to S/m.

$$\frac{200 \ micro-S}{cm} \quad \frac{1 \ micro-S}{1x10^6 S} \quad \frac{100 \ cm}{1 \ m} = 0.02 \frac{S}{m}$$

$$Resistivity = \frac{1}{Conductivity} = \frac{1}{0.02 \frac{S}{m}} = 50 \ ohm - m \rightarrow the \ inverse \ of \ Seimens \ is \ ohm$$

Solution to Activity 2

The predicted inversion result is blurry and blunt compared to the true model. The top is relatively well resolved, the sides less so, and the bottom is poorly resolved. The estimated resistivity does not capture all of the contrast between the background resistivity (500 ohm-m) and the cavity resistivity (50 ohm-m); the minimum value estimated inside the cavity is about 370 ohm-m compared to 50 ohm-m.
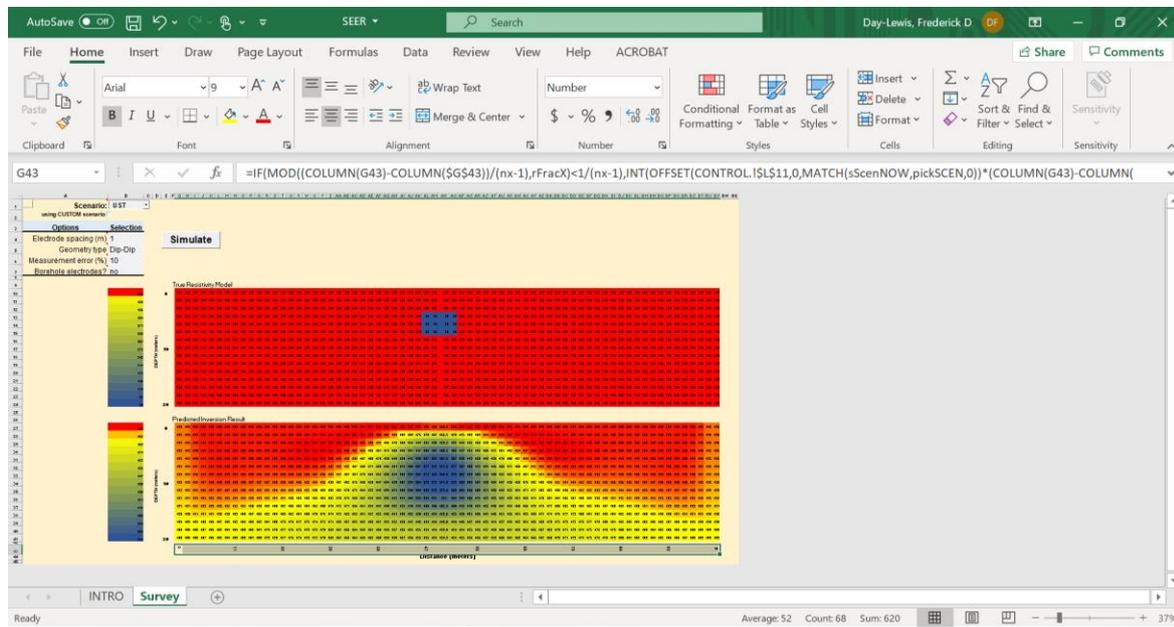
Solution to Activity 3

By assuming a smaller measurement error of 1%, the general pattern is the same, but the estimated resistivity is closer to the actual resistivity of the target, with a minimum estimated resistivity of ~320 ohm-m.

64

Solution to Activity 4

Changing the survey type to 'Combined' results in the same general pattern of estimated resistivity, so one concludes that adding Wenner measurements alone does not improve the results sufficiently to warrant the additional field effort.

Solution to Activity 5

The addition of borehole electrodes and associated crosshole measurements greatly improves the resolution of the cavity. The boundaries of the target are more precisely located, perhaps to +/- 1 m, and the magnitude of the anomaly is better captured, with an estimated resistivity showing a minimum of about 100 ohm-m.

10   Exercise Solutions

Solution Exercise 1

Resistivity is an intrinsic property of a material and describes how difficult it is for electrical current to flow through that material. Electrical resistivity is the reciprocal of electrical conductivity. Electrical resistivity is therefore analogous to the reciprocal of hydraulic conductivity (*K*).

Resistance is also a measure of the difficulty with which electrical current can flow, but it is dependent on geometry. It is similar to transmissivity, which is dependent on hydraulic conductivity and layer thickness, but when resistance to current flow is measured, it depends on resistivity of the material, the distance between the measurement points, and the cross-sectional area through which current is flowing between those points. In 1-D current flow (e.g., in a wire, or column of uniform properties), resistance is directly proportional to length between the ends of the column and inversely proportional to the cross-sectional area of the column. The equivalent hydraulic parameter would be the hydraulic resistance, or $L/(KA)$, where *L* is the length of the flow path and *A* is the cross-sectional area through which water flows. Consequently, because of this geometric dependence, resistance values can be small or large—even in a system with homogeneous resistivity.

Apparent resistivity applies a geometric factor to the measured resistance to estimate what the resistivity of the system would be, assuming a homogeneous Earth extends infinitely with depth and lateral distance. Only in the case of a homogeneous Earth will the apparent resistivity equal the true resistivity. The utility of apparent resistivity is that it allows a practitioner to look at their field data to see if the values are reasonable and to rapidly locate anomalies. Inversion of the data is required to obtain actual resistivity values.

Return to Exercise 1

Solution Exercise 2

Darcy's law is defined by $q = -K\nabla h$, where:

q = specific discharge (length/time)

∇h = head gradient (length/length)

K = hydraulic conductivity (length/time)

Ohm's law is defined by $J = -\sigma\nabla V$, where:

J = current density (Ampere/length^2)

∇V = voltage gradient (voltage/length)

σ = electrical conductivity (Seimens/length)

The electrical current density quantifies the flow of electric charge and is thus equivalent to the flow of water. Head and voltages are both measures of potential (or energy). Electrical conductivity controls how easily current can flow through the medium, like water with hydraulic conductivity. When combined with conservation of mass or charge, both of these equations become diffusion equations.
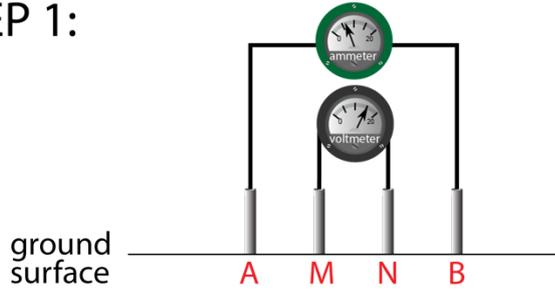
Return to Exercise 2

Solution Exercise 3

a. Dead battery: Batteries are sold by the potential difference they maintain and by the amount of electricity (charge) they can deliver. This is equivalent to the height of water behind a dam, and the volume of water that can be released. A dead battery is thus like an empty reservoir.

b. Short circuit: A short circuit occurs when there is a highly electrically conductive pathway across a circuit, shortcutting current flow. The closest analogy in hydrology might be a conductive fracture, which could shortcut flow across an otherwise extremely low permeability rock.

c. Open circuit: An open circuit exists when electric current cannot traverse the entire circuit e.g., if there is a break in the power cord leading to a hair dryer. This would be equivalent to a truly impermeable block of material that water could not move through.

d. Voltmeter: A voltmeter measures a drop in electrical potential in an electric circuit. Heads are the equivalent potential term in hydrology and are measured by a water-level tape (physical or electrical), pressure transducer, a sonic device, or something similar. Of course, a voltmeter and a water-level tape aren't entirely equivalent. A water-level tape just measures the head at one location. With electricity, we are always looking at differences in voltage. A voltmeter is the electrical equivalent of measuring the head difference between two wells. While in both cases, differences in potential are what drive flow, with heads, we can set a datum and make individual measurements relative to the datum, while with current we need to capture the voltage difference in one measurement.
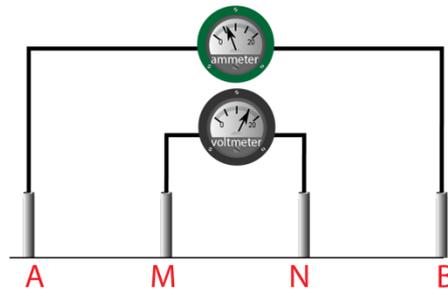
Return to Exercise 3

Solution Exercise 4

Field layout for a 1D resistivity sounding:
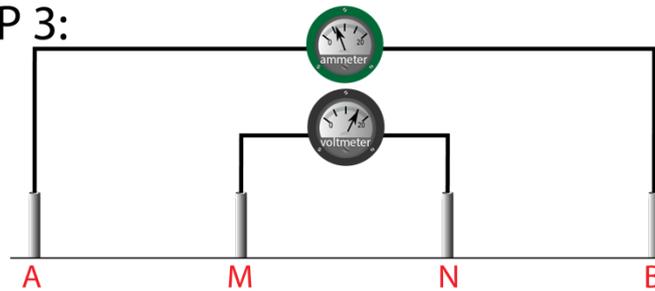
STEP 1:

STEP 2:

STEP 3:

and so on, with incrementally larger distances.

Return to Exercise 4

Solution Exercise 5

Calculate the apparent resistivity in the following arbitrary electrode configuration when a 5 mA current is injected between electrodes *A* and *B,* and 80 mV is measured between *M* and *N*.

$$K_g = \frac{2\pi}{\frac{1}{\overline{AM}} - \frac{1}{\overline{AN}} - \frac{1}{\overline{BM}} + \frac{1}{\overline{BN}}}$$

$$= \frac{2\pi}{\frac{1}{2m} - \frac{1}{3m} - \frac{1}{4m} + \frac{1}{3m}}$$

$$= 25.1 \ m$$

$$\rho_a = K_g(\Delta V / I)$$

$$= 25.1 \ m * 80 \ mV / 5 \ mA$$

$$= 400 \ \text{ohm-m}$$

Return to Exercise 5↴

Solution Exercise 6

Current injected [I]: 2 mA

Apparent resistivity [ρ]: 250 ohm-m

Noise level: 15 mV

$$K_g = \frac{2\pi}{\frac{1}{\overline{AM}} - \frac{1}{\overline{AN}} - \frac{1}{\overline{BM}} + \frac{1}{\overline{BN}}}$$

$$K_{g,Wenner} = \frac{2\pi}{\frac{1}{5m} - \frac{1}{10m} - \frac{1}{10m} + \frac{1}{5m}}$$

$$= 31.4 \ m$$

For a positive geometric factor with a dipole-dipole array, you need to have the electrodes configured as $A\ B\ N\ M$ (this also gives a positive resistance). If you configure the electrodes as $A\ B\ M\ N$ (as often written) the geometric factor is negative (so is the resistance). Using $A\ B\ N\ M$ the geometric factor is:

$$K_{g,dipole-dipole} = \frac{2\pi}{\frac{1}{\overline{AM}} - \frac{1}{\overline{AN}} - \frac{1}{\overline{BM}} + \frac{1}{\overline{BN}}} = \frac{2\pi}{\frac{1}{9m} - \frac{1}{6m} - \frac{1}{6m} + \frac{1}{3m}} = 56.5 \ m$$

If you do the calculation as $A\ B\ M\ N$, you get a geometric factor of -56.5.

We then need to calculate the apparent resistivity:

$$\rho_a = K_g \Delta V / I$$

ρ_{a_Wenner} = 250 ohm-m = $\frac{31.4 \ m \ V \ mV}{2 \ mA}$

solving for V yields V = 15.9 mV

$\rho_{a\_dipole\text{-}dipole}$ = 250 ohm-m = $\frac{56.5 \ m \ V \ mV}{2 \ mA}$

solving for V yields V = 8.8 mV

A negative voltage would be correct for $A\ B\ M\ N$ configuration, as the geometric factor is negative.

In summary:

Array	a(m)	n	K_g	V(mV)	SNR
Wenner	5	-	31.4	15.9	1.06
Dipole-dipole	3	3	56.5	8.8	0.59

Solution Exercise 7

The ER inversion process, involves estimating parameter values for the starting model and simulating the field measurements, then comparing the simulated values to the field data, and if there is a good fit then the inversion process is stopped and the current parameter values are used, while if not, the parameter values are updated and the process is repeated until an acceptable fit is reached.
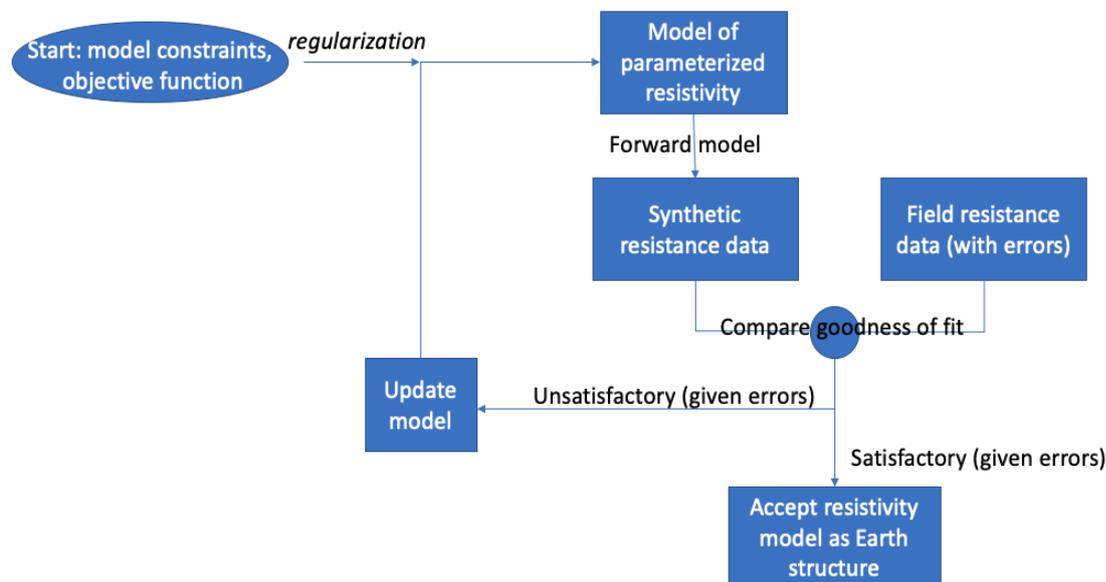
Solution Exercise 8

There are multiple reasons why the model for the conductivity of the earth below an array of electrodes is likely to deviate from reality. Four reasons are:

1. Measurement physics: electrical conduction is described by a diffusion equation; small-scale heterogenieties are often not captured by these equations
2. Parameterization and regularization: as part of the inverse problem, the mathematics describing electrical flow is discretized, leading to some errors, and regularization is added to the inverse problem that often serves to smooth the final image
3. Limited resolution: there is insufficient information in the data to capture all the heterogeneity of the subsurface
4. Measurement errors: due to a variety of often unavoidable issues in the field

11   About the Authors

Dr. Kamini Singha is a Professor in the Department of Geology and Geological Engineering and Associate Dean of Earth and Society Programs at Colorado School of Mines in Golden, Colorado, USA. She has a Ph.D. in Hydrogeology from the Department of Geological and Environmental Sciences at Stanford University in 2005 and a Bachelor of Science degree with Honors in Geophysics from the Department of Geology and Geophysics at the University of Connecticut in 1999.

Her research interests rely on fluid flow and solute transport in porous media and fractured rock as well as groundwater-surface-water interactions; integration of hydrologic and geophysical techniques; quantification of the "geophysical footprint" to constrain the operation of parameters controlling fluid flow and solute. She has worked a wide variety of multidisciplinary problems including imaging tree water use with electrical geophysics; mapping water quality degradation and its connections to human behavior; imaging moisture dynamics in desert ecosystems; exploring changes in infiltration after fire; and quantifying kinetics of iron reduction given electrical measurements.

Dr. Singha is an award-winning teacher, a recipient of a U.S. National Science Foundation CAREER award and the Early Career Award from the Society of Environmental and Engineering Geophysics, a Geological Society of America Fellow, and a former Fulbright Scholar. She served as the U.S. National Groundwater Association's Darcy Lecturer in 2017, and is a current Editor at Water Resources Research.

She currently teaches Groundwater Engineering, Geological Data Analysis, and Field Methods in Hydrology at the Colorado School of Mines. For a full, up-to-date list of her publications, please [click here↗](#).

Dr. Timothy C. Johnson is a computational scientist in subsurface geophysical imaging and interpretation related to complex environmental challenges and energy applications. He is nationally and internationally recognized for his work in electrical resistivity tomography (ERT) as a characterization and monitoring technology. He pioneered the development of E4D-RT, a real-time, four-dimensional subsurface imaging software that allows scientists to "see" subsurface processes and solutions in real-time. He and his team received a prestigious R&D 100 Award in 2016 for this tool. He joined Pacific Northwest National Laboratory in 2010 as a senior research scientist. He worked at Idaho National Laboratory from 2007-2010 and, before that, was a staff engineer at

73

American Geotechnics. He is focused on joint inversion of multiple geophysical techniques using parallel computing to improve time-lapse imaging.

Dr. Johnson has a Doctorate degree in Geophysics in 2006, a Bachelor's degree in Civil Engineering in 2001, and a Bachelor's degree in Geophysics in 1999, all from Boise State University. He has received awards and recognitions, including: Laboratory Director's Award for Exceptional Engineering Achievement in geophysical imaging, 2017; R&D 100 Award for Real-Time Four-Dimensional Subsurface Imaging Software (E4D-RT - (https://e4d.pnnl.gov↗) in 2016; and R&D Magazine honor for inventors of 100 most technologically significant products each year. He has the U.S. Patent No. 9,772,423, September 26, 2017, "Method Of Imaging The Electrical Conductivity Distribution Of A Subsurface". The full list of his publications can be found here.

The bulk of Dr. Johnson's research has been commissioned by the U.S. Department of Energy and Department of Defense, focusing on developing joint geophysical methods for investigating shallow subsurface contamination issues, for understanding stress and fluid flow in deep crystalline rock systems, and for understanding the effects of underground explosions.

Dr. Frederick D. Day-Lewis a Chief Geophysicist and Laboratory Fellow with the Pacific Northwest National Laboratory's Earth Systems Science Division. He received a Ph.D. in Hydrogeology from Stanford University (2001) and a Bachelor of Science and Bachelor of Arts in Hydrology and English from the University of New Hampshire (1994). Prior to starting at Pacific Northwest National Laboratory, he was a Research Hydrologist at the U.S. Geological Survey, where he developed and applied hydrogeophysical methods in groundwater studies across the U.S. Dr. Day-Lewis conducts applied research on characterization, monitoring, and understanding of hydrologic processes, with current emphases on groundwater/surface-water interactions and fractured rock. Recent activities include studies to improve the understanding of hyporheic zone processes and measurements of properties controlling contaminant storage in geologic materials. He has experience using electrical, radar, and electromagnetic geophysical methods as well as distributed temperature sensing. In this work, he also develops software for improved analysis and visualization of related data (1DTempPro, DTSGUI, FLASH-R). As part of his technology transfer efforts, Dr. Day-Lewis collaborates with state and federal partners including SERDP, ESTCP, DOE, EPA, and others to support informed decision-making on the selection and application of hydrogeophysical tools and methods. He also develops decision support tools (SEER, FRGT-MST) to help practitioners and environmental site managers identify near-surface geophysical methods appropriate for a given project's goals and site conditions.

Dr. Day-Lewis co-edited the American Geophysical Union monograph "Subsurface Hydrology: Data Integration for Properties and Processes" (2007). He is a Fellow of the Geological Society of America, past President of the American Geophysical Union's Near Surface Geophysics Section, and past Vice President of the Environmental and Engineering Geophysical Society. He has served as an Associate Editor for Water Resources Research, Groundwater, Hydrogeology Journal, and Geosphere.

Dr. Lee D. Slater, after study in the United Kingdom, a postdoctoral appointment, and initial tenure-track faculty position in the U.S., joined Rutgers University in 2002 to continue performing research in hydrogeophysics. He is currently a Henry Rutgers Professor in Geophysics at Rutgers University Newark and an internationally recognized expert in near-surface geophysics and hydrogeophysics. His research is primarily focused on the use of electrical geophysical technologies for subsurface characterization and monitoring. He has published extensively, including 150 papers in peer-reviewed international journals of hydrogeology and geophysics, as well as being a co-author of the recent book "Resistivity and Induced Polarization: Theory and Applications to the Near Surface Earth".

Dr. Slater has served as principal investigator on multiple research and technology demonstration projects funded by the U.S. Department of Defense, U.S. Department of Energy, U.S. Department of Agriculture, U.S. National Parks Service, and National Science Foundation. He has also served in prominent leadership roles in the academic geophysical community, including Chair of the Near Surface Geophysics Focus Group of the American Geophysical Union (AGU), Chair of the AGU Hydrogeophysics Technical Committee, and President of the Environmental and Engineering Geophysical Society (EEGS).

Dr. Slater currently serves as Associate Editor of Water Resources Research (WRR) and he recently edited a new volume on Near Surface Geophysics published in the 2nd Edition of the Treatise on Geophysics, part of the Elsevier Major International Reference series. He has served on multiple advisory boards for large interdisciplinary hydrogeological research projects in Europe.

He was the recipient of the 2013 Harold B. Mooney award of the Society of Exploration Geophysicists (SEG). His numerous Ph.D. graduates have mostly gone onto academic positions and are now making their own contributions to advancing research in hydrogeophysics. In 2018 Dr. Slater was elected Fellow of the American Geophysical Union (AGU), with the citation: "for visionary experimentation in near-surface geophysics that has advanced understanding of subsurface hydrogeological and biogeochemical processes".

Please consider signing up to the GW-Project mailing list and stay informed about new book releases, events and ways to participate in the GW-Project. When you sign up to our email list it helps us build a global groundwater community. Sign up↗.

Modifications to Original Release

Changes from the Original Version to Version 2

Original Version: December 2021, Version 2: August 2022

General changes:

Seven links to Figures in the original book showed an error message instead of the figure number. These were corrected and the table of contents was updated to accommodate any page number changes that occurred given the substitution of the figure label for the error statement.

Changes from Version 2 to Version 3

Version 3: 9 March 2023

General changes:

removed Table of Figures as per updated Groundwater Project book format

major sections now start on a new page as per updated Groundwater Project book format

parameters that were not in italic font were changed to italic font

units that were in italic font were changed to standard font

updated Table of Contents

Specific Changes:

page numbers refer to the pdf of version 2

page ii, added Version 3

page iii, updated copyright format and added doi, updated number of pages, changed to APA 7th edition format for citation, added "of" after "example in description of the cover image

page ix, corrected two misspellings of imaging from imagining in the foreword

page 4, 1st paragraph, 4th line from bottom, units Ω.m corrected to Ω-m

A

page 5, after Equation 1, first letter of parameter definitions changed to lower case unless proper nouns as per Groundwater Project book format

page 5, added units of meters to definition of x_s, y_s, z_s

page 8, Equation 5, a close parenthesis ') ' was added to the end of the righthand side

page 12, caption of Figure 4, J' is now defined as J's transpose

page 27, in equation 9a, C_D^{-1} was corrected to $C_D^{-0.5}$

page 27, deleted 'is the' in definition of D

page 28, removed variable $d_{sim,i}$ from variable definitions because it does not appear in Equation 10a or 10b

page 29, definitions after equation 11, variable a changed to a_i

page 31, Equation 12b, 100* changed to 100%

page 34, end of third to last sentence of Section 4.5, Figure 2 changed to Figure 4 and the errant image of Figure 2 at that location was removed

page 34, last sentence of Section 4.5, added () around 2014

page 54, cCaterina changed to Caterina

page 64, title of Section 10, Exercises changed to Exercise

page 65, definition of Darcy's Law, variable k changed to upper case K

page 65, definition of K dimensions changed from (length time) to (length/time)

page 69, added overbars to AM, AN, BM, BN in equation for $K_{g,dipole\text{-}dipole}$

page 69, added m after 56.5 at end of equation for $K_{g,dipole\text{-}dipole}$

page 69, presented ρ_{a_Wenner} and $\rho_{a\_dipole\text{-}dipole}$ as stacked fractions to facilitate reading

Changes from Version 3 to Version 4

Version 4: 15 March 2023

<u>Specific Changes:</u>

B

page numbers refer to the pdf of version 3

page ii, added Version 4

page 13, in the caption of Figure 4, changed:
    and *J′* is its transpose, which is
    to:
    and *J′* is its transpose. The Jacobian matrix is

C